Mutational order and epistasis determine the consequences of *FBXW7* mutations during colorectal cancer evolution

Dedrick Kok Hong Chan[1,2], Amit Mandal[1], Scott David Collins[1], Yi Zhou[1], Richard Owen[3], James Bundred[1], Jacob Household[4], Trevor A Graham[4], Xin Lu[3], Simon James Alexander Buczacki[1]

[1] Nuffield Department of Surgical Sciences, University of Oxford, Oxford, United Kingdom

[2] NUS Centre for Cancer Research, Yong Loo Lin School of Medicine, Singapore

[3] Ludwig Institute for Cancer Research, Nuffield Department of Medicine, University of Oxford, Oxford, United Kingdom

[4] Centre for Evolution and Cancer, The Institute of Cancer Research, London, UK.

Running title: *FBXW7* and mutational order in CRC evolution

Correspondence: simon.buczacki@nds.ox.ac.uk

Abstract

Somatic driver mutations, in genes such as *FBXW7,* have been discovered in phenotypically normal colonic tissue, however their role in cancer initiation remains elusive. Here, using patient-derived human colon organoids as models of early tumour evolution we investigate the consequences of *FBXW7* mutations in normal and gene-edited organoids. We observed that *FBXW7* mutations exert an epistatic effect where the transcriptional consequences of the mutation are dependent on the background mutational makeup of the cell. Specifically, we found the timing of acquiring an *FBXW7* mutation relative to *APC* mutation, led to profound differences. When *FBXW7* was mutated before *APC*, repression of the *APC* transcriptional response and maintenance of near-normal cell state was seen. However, when *APC* was mutated before *FBXW7*, cells acquired classic cancer-stem cell features. Single-cell RNA sequencing revealed that *FBXW7* mutations in normal tissue also function by subtly reordering stem cell hierarchies and priming a fetal/regenerative phenotype through upregulation of YAP/TAZ signaling. Further analysis using transposase-accessible chromatin sequencing found this cellular plasticity was driven by changes in the chromatin accessibility of 36 transcriptional start site regions associated with TEAD1/TEAD2 motifs, which in turn upregulated YAP. Taken together, we demonstrate a critical role of *FBXW7* mutations in preventing the initiation of colorectal cancer, and provide exemplar evidence for the importance of epistasis and mutational order in cancer biology.

Introduction

Somatic mutations have been detected in a range of normal human tissues, including the liver [1], esophagus [2], skin [3], and endometrium [4]. Similarly, a catalogue of somatic mutations in normal human colonic epithelium has been uncovered using whole genome sequencing of two thousand crypts, strikingly finding mutated cancer genes in phenotypically normal colonic epithelium; here termed 'normal drivers' [5, 6]. Within this list of normal drivers is the gene of interest in this study, *FBXW7*. In the normal colon, normal drivers form a distinct category from cancer drivers such as *TP53* or *APC*, which are ubiquitously found in colorectal cancer. Instead, normal drivers possess a hitherto unknown role in cancer initiation. FBXW7 is a key component of the Skp1-Cdc53/Cullin-F-box-protein complex (SCF/β-TrCP), an E3 ubiquitin ligase responsible for marking proteins by ubiquitination, targeting them for proteasomal degradation [7]. Substrates of FBXW7 are key regulators of cellular gene transcription, cell cycle progression or activators of signaling pathways, thus making *FBXW7* a key tumour suppressor gene. The significance of *FBXW7* mutations in the context of normal tissues however remains uncharacterized. Given normal driver genes such as *FBXW7* acquire mutations before the acquisition of accepted initiating mutations associated with colorectal cancer such as *APC*, *TP53*, *SMAD4* or *KRAS*, raises the possibility that normal driver mutations could be anticipated to play a critical role in early cancer evolution. Furthermore, the timing of the *FBXW7* mutation preceding known cancer drivers suggests that the order of mutation acquisition may have important effects on phenotype.

Recently, there has also been significant interest in the effects of epigenetic plasticity in cancer evolution. In models of early pancreatic cancer, *KRAS*-mutant cells were shown to demonstrate distinct chromatin accessibility patterns which could predict divergence into either a benign or malignant fate [8]. In colorectal cancer, the impact of epigenetic changes on tumour initiation are beginning to be uncovered. Johnstone et al. highlighted the importance of the three-dimensional architecture, in the form of chromatin loops, topologically activating domains and large-scale compartments, of DNA in restricting malignant progression [9]. A more recent study by Heide et al.

found chromatin modifier genes are actively mutated in the early initiation of colorectal cancer, and can result in the accumulation of further genetic mutations which herald carcinogenesis [10].

In this study, we used adult human colonic organoids and CRISPR-Cas9 gene editing to explore the cell autonomous and gene-interactive effects of an *FBXW7* mutation. Combining gene editing with organoid culture fashions a powerful tool ideal for studying the functional consequences of driver mutations in normal tissue for it allows specific mutations to be introduced into tissue devoid of genetic perturbation. By sequentially introducing multiple distinct mutations in the same cell, we also aimed to determine relationships arising between cells with an *FBXW7* mutation and the acquisition of subsequent cancer driver mutations. We found that cells with an *FBXW7* mutation were transcriptionally similar to wildtype cells but subtly primed towards a foetal/YAP-active state. Further, we observed that an initial *FBXW7* mutation dampened the transcriptional effect of a subsequent *APC* mutation also resulting in retention of a near-wildtype phenotype. Whereas when we reversed this order of mutations, despite identical genotype, we generated *bona fide* cancer organoids. We uncovered this profound mutational order-based cellular plasticity to be driven by epigenetic differences in both global and local chromatin accessibility. Here we provide the first direct eukaryotic evidence for the existence of epistasis, and that order of mutations, as much as the mutations themselves, are key in determining their effect.

Results

Mutant *FBXW7*$^{-/-}$ recapitulate known effects on downstream targets

Patient-derived adult stem cell wildtype organoids (W) were generated from phenotypically normal colon tissue of patients undergoing surgery for colorectal cancer. CRISPR-Cas9 editing was used to generate *FBXW7*$^{-/-}$ organoids (F) [11]. Our gene editing strategy utilizes three sgRNAs to introduce large deletions at exon 2 of the *FBXW7* gene. F and W organoids possessed similar morphology (Fig. 1a). We validated knockout of the *FBXW7* gene using western blot (Fig. 1b), as well as immunofluorescence using anti-FBXW7 antibodies (Fig. 1c). We performed western blot on the

99 substrate targets of FBXW7: p-c-Jun, cyclin E, p-c-Myc, and Notch intracellular domain (NCID) and
100 showed upregulation of all protein substrates on knockout of FBXW7 (Fig. 1d).

101 To characterise transcriptional differences between F and W organoids, we performed bulk-RNA
102 sequencing (RNA-seq) on both organoid types (Fig. 1e). Using a cut-off of $\log_2 FC \leq -1.5$ or ≥ 1.5, and
103 adjusted p-value < 0.05, F and W were transcriptionally similar with only two genes found
104 differentially expressed.

105

106 *FBXW7*$^{-/-}$ mutants do not exhibit a competitive proliferative advantage over wildtype organoids

107 Given the transcriptional similarities between W and F organoids, we interrogated the possibility of a
108 competitive or cooperative effect by co-culturing F organoids with W organoids. This follows from
109 our earlier work in CRC cell lines where we had shown DNA damage via an AKAP8-mediated
110 mechanism in wildtype cells adjacent to *FBXW7*$^{-/-}$ cells [12]. Similarly, murine *Apc*$^{-/-}$ intestinal
111 organoids co-cultured with wildtype organoids have been shown to demonstrate increased
112 proliferation as a result of a supercompetitor effect driven by secretion of the Wnt-antagonist
113 NOTUM from *Apc*$^{-/-}$ organoids [13]. As a positive control for our co-culture model, we therefore
114 generated human *APC*$^{-/-}$ organoids (A) and performed lentiviral transduction of A organoids with
115 pCDH-CMV-mCherry-T2A-Puro (Addgene #72264). W organoids underwent lentiviral transduction
116 with pCDH-EF1-copGFP-T2A-Puro (Addgene #72263). A and W organoids were co-cultured in equal
117 proportion, and fluorescent imaging was performed on days 1, 3, 5 and 7 (Extended data figure 1a). In
118 A and W co-cultured organoids, mCherry-labelled A organoids demonstrated a significant
119 proliferative advantage in concordance with previously described results performed in murine
120 organoids (Extended data figure 1c and d). F organoids were co-cultured with W organoids in a
121 similar fashion. F organoids underwent lentiviral transduction with pCDH-CMV-mCherry-T2A-Puro
122 (Addgene #72264). In F and W co-cultured organoids, proliferation in both F and W organoids did not
123 exhibit any differences (Extended data figure 1b, e and f). This was confirmed by an EdU

124 proliferation assay which showed no difference in EdU positive cells between F and W organoids
125 grown separately (Extended data figure 1g).

126 We sought to determine whether F mutants exerted a transcriptional effect on co-cultured W
127 organoids. In F and W co-cultured organoids, we performed fluorescent activated cell sorting (FACS)
128 to isolate GFP and mCherry positive cells, representing W and F cells respectively. Sorted cells were
129 submitted for bulk-RNAseq, and the transcriptome compared to non-co-cultured cells. Again, we
130 observed that transcriptomes between co-cultured W and non-co-cultured W (Extended data figure
131 1h), and co-cultured F and non-co-cultured F organoids (Extended data figure 1i) exhibited minimal
132 differences. Taken collectively, our findings suggest that there is minimal effect of F organoids on
133 neighbouring W cells, in contrast to our earlier findings in cell lines [12].

134

135 *FBXW7* mutation provides evidence of epistasis

136 In light of the lack of a cooperative/competitive interaction with wildtype cells, and building on our
137 earlier finding that F organoids were transcriptionally similar to W organoids, we generated an
138 organoid model mirroring the polypoidal and cancerous phases of CRC carcinogenesis (Figure 2a).
139 An $APC^{-/-}$ mutation introduced into W organoids generated A organoids, representing the polypoidal,
140 precancerous phase, while a $TP53^{-/-}$ mutation introduced into A organoids, therefore possessing a
141 double knockout $APC^{-/-}$ / $TP53^{-/-}$ mutation, generated AT organoids and representing the cancerous
142 phase. On each of these A and AT organoids, an *FBXW7* mutation was then introduced, generating AF
143 and ATF organoids respectively (Figure 2b).

144 As previously described, A organoids were morphologically distinct from W organoids [14, 15]. A
145 organoids grew large and cystic. The subsequent acquisition of a *TP53* mutation preserved this
146 phenotype. Importantly, an additional *FBXW7* mutation on both the A and AT organoids also
147 maintained this cystic morphology. To further characterise transcriptional differences between these
148 different organoids, A, AF, AT and ATF organoids were submitted for bulk-RNAseq. A organoids were
149 compared with AF organoids, while AT organoids were compared with ATF organoids. We observed

150 an epistatic effect of the *FBXW7* mutation in our comparison of various groups. Together with our
151 earlier comparison between F and W organoids which saw only 2 differentially expressed genes, we
152 observed 87 differentially expressed genes between A and AF, and 294 between AT and ATF (Figure
153 2c, and Extended data figure 2a and 2b). Hierarchical clustering of these different groups showed that
154 F and W organoids clustered together, while A, AF and ATF organoids formed separate clusters
155 (Figure 2d). These results demonstrate that the same *FBXW7* mutation can have varying effects
156 depending on its mutational background. More importantly, it suggests that an *FBXW7* mutation may
157 have different cellular effects depending on when the mutation was acquired, and that an early
158 mutation will have fewer effects compared with a later mutation.

159 To ensure observations were not an artifact of repeated iterations of gene editing, we targeted the
160 *AAVS1* safe harbour locus three times to replicate the triple-mutant ATF organoids. Morphologically,
161 *AAVS1*-targetted organoids resembled wildtype organoids (Extended data figure 3a). Bulk-RNAseq of
162 *AAVS1*-targetted organoids compared with W organoids showed only two differentially expressed
163 genes with a cut-off of $\log_2 FC \leq -1.5$ or ≥ 1.5, and adjusted p-value < 0.05 (Extended data figure 3b),
164 greatly differing from the 493 differentially expressed genes between ATF and W organoids
165 (Extended data figure 3c). These findings confirm that epistatic effects described earlier were not
166 simply a function of repeated iterations of CRISPR-Cas9 gene editing.

167

168 Order of *FBXW7* mutation determines its transcriptional effect

169 To ascertain the transcriptional effect of the order of mutation, we designed an experiment in which
170 organoids possessed the same mutations, but differed in the sequence in which the mutations were
171 introduced. As previously described, AF organoids possessed an *APC* mutation, followed by an
172 *FBXW7* mutation. We generated FA organoids, which acquired an *FBXW7* mutation prior to the *APC*
173 mutation (Fig. 3a). Morphologically, FA organoids did not acquire the cystic phenotype characteristic
174 of A or AF organoids (Fig. 3b). We submitted AF and FA organoids for bulk-RNAseq. Principal
175 component analyses of AF and FA organoids gene expression, together with W, A and F organoids

176 revealed that FA organoids did not cluster with AF organoids (Fig. 3c). Instead, FA organoids
177 clustered with F and W organoids, while AF organoids clustered with A organoids. To further analyse
178 the transcriptional effect of changing the order of mutations, we used a cut-off of $\log_2FC \leq -0.7$ or $\geq$
179 0.7 to identify differentially expressed genes when AF and FA organoids groups were compared with
180 wildtype organoids. This cut-off selected for 3335 genes in the AF group and 861 genes in the FA
181 group (Figure 3d). As expected, there was significant overlap in the genes which were differentially
182 expressed in both groups. In the FA group, 628 (72.9%) genes were also differentially expressed in the
183 AF organoids. Further analyses of the gene expression changes for these 628 genes suggested a
184 dampening effect of an earlier *FBXW7* mutation, such that the magnitude of the transcriptional
185 perturbation was rendered less positive or negative (Figure 3e). Using GSEA, we also observed that
186 some key signaling pathways involved in carcinogenesis such as the EMT pathway were significantly
187 more active in FA compared with AF organoids (Normalised enrichment score (NES) 2.21, adjusted
188 p-value= 1.70×10^{-10}). Collectively, these findings promulgate our observation that mutational
189 background affects the transcriptional effect of a mutation. Moreover, our findings also suggest that
190 *FBXW7* mutations in normal tissue may protect against the future effect of an *APC* mutation, and by
191 extension, could be protective against the initiation of CRC.

192

193 scRNAseq data suggests dedifferentiation towards a fetal state in *FBXW7* mutant organoids

194 We endeavored to explain our finding that an *FBXW7* mutation was protective to consequences of a
195 later acquisition of an *APC* mutation, considering our observation that mutational order affects
196 transcriptomic expression. We hypothesized that subtle transcriptomic changes could be present in F
197 organoids in small subpopulations of cells which might be masked by bulking during RNAseq. To
198 overcome this, we performed single-cell RNA sequencing (scRNAseq) on F and W organoids.
199 Clustering by Uniform Manifold Approximation and Projection (UMAP) showed 14 clusters (Fig.
200 4a). Notably cluster 13 was unique to *FBXW7* mutant cells (Fig. 4b). This cluster was marked by
201 genes such as *KRT17* ($\log_2FC$= -1.65, p= 2.52×10^{-35}), *TAGLN* ($\log_2FC$= -1.33, p= 2.81×10^{-35}), and
202 *MMP7* ($\log_2FC$= -1.47, p= 7.70×10^{-34}) and an EMT signature (Extended data figure 4). Importantly,

203 we observed that wildtype cells expressed *FBXW7*, indicating that this gene is expressed in normal
204 epithelium (Fig. 4c). Analysis by RNA velocity indicated that cluster 13 was an important terminal
205 differentiation state, which could only have occurred in *FBXW7* mutant cells (Fig. 4d). As expected,
206 quantitative analysis between UMAP plots from F and W organoids demonstrated a statistically
207 significant upregulation of the FA_up gene signature in F organoids relative to W organoids (Fig. 4e).
208 We also observed increased expression of fetal gene signature [16] (Fig. 4f), and the YAP pathway
209 gene signature [17] (Fig. 4g) in F organoids. There was also a decreased expression of the intestinal
210 stem cell signature (ISC) [18] (Fig. 4h), and decreased expression of the crypt-based columnar (CBC)
211 stem cell signature [19] (Fig. 4i) in F organoids. We re-analysed bulk RNAseq data comparing F and
212 W organoids using gene set enrichment analysis and found that fetal (Extended data figure 5a) and
213 YAP (Extended data figure 5b) signatures correlated with our scRNAseq results. We observed a
214 downregulation of the ISC (Extended data figure 5c) and CBC (Extended data figure 5d) signatures in
215 bulk RNAseq as in scRNAseq, though this did not achieve statistical significance. In contrast, we did
216 not observe an FA_up gene signature in our bulk RNAseq comparison of F versus W (Extended data
217 figure 5e), which could be a function of minimal transcriptional perturbation observed in F organoids
218 compared with W organoids. To further explore the YAP pathway, we performed additional GSEA on
219 FA vs W and AF vs W organoids. Intriguingly, this showed greater enrichment of the YAP signature in
220 FA vs W (ES= 0.58) (Extended data figure 6a) compared to AF vs W (ES= 0.36) (Extended data
221 figure 6b). Taken together, these findings point towards a reordering of the stem cell hierarchy,
222 favouring pathways which recall a fetal regenerative/YAP active cell state.

223

224 Transcriptional effects of mutational order are driven by local and global changes in chromatin
225 accessibility

226 We then sought to uncover the mechanism which resulted in FA and AF organoids exhibiting such
227 profound transcriptional differences despite identical genotypes. We hypothesized that changes in
228 chromatin accessibility induced by the earlier acquisition of an *FBXW7* mutation could influence the
229 effects of a subsequent *APC* mutation. To interrogate this, we performed assay for transposase-

230 accessible chromatin with sequencing (ATACseq) on W, FA and AF organoids. In total, 14 543 peaks
231 differed between AF and W organoids, 16 990 peaks differed between FA and W organoids, and 2 156
232 peaks differed between AF and FA organoids. Reassuringly, these findings suggest that there was
233 much similarity in the effect of mutational order on chromosome accessibility between AF and FA.
234 More importantly, we noted that the overall accessibility of the whole genome was reduced in FA vs
235 W organoids compared with AF vs W organoids (Figure 5a). Concordant with scRNAseq analysis
236 between F and W organoids, we observed that there was increased accessibility to genes in the CBC
237 signature in AF vs W organoids compared with FA vs W organoids (Figure 5b). We performed *de*
238 *novo* transcriptional factor motif scan using the GADEM algorithm on ATAC-seq peaks from AF vs
239 W and FA vs W organoids. Two de novo motifs found enriched in the FA vs W organoid comparison
240 included “nCwGCmCwGn” (Figure 5c) and "rGCAGGTGn” (Figure 5d). The top 3 closest matches
241 to each of these motifs as per JASPAR database, were *ZNF449*, *TEAD2*, and *TEAD1* and *SNAI1*,
242 *SCRT2*, and *CTCFL* respectively. Intriguingly, TEAD1 and TEAD2 motifs were more accessible in
243 FA vs W organoids relative to AF vs W organoids (Figure 5e). The TEAD transcriptional factor is the
244 main regulatory factor for the Hippo signaling pathway [20], which in turn activates YAP and TAZ.
245 This concurs with our scRNAseq analysis of F organoids which showed an upregulation of YAP
246 pathway gene signature. We also observed increased chromatin accessibility of FA vs W organoids
247 compared with AF vs W organoids at the SNAI1 transcription factor motif (Figure 5f), which
248 mediates EMT by repressing E-cadherin expression, therefore concurring with results observed in
249 bulk RNAseq and scRNAseq analysis of differentially expressed pathways. Taken together, our
250 findings strongly implicate an epigenetic mechanism in which an early *FBXW7* mutation results in
251 transcriptional quiescence, and represses the effect of a later *APC* mutation.

252

253 Effects of our observed timing of mutation are recapitulated in patient data

254 To perform patient validation of our findings, we turned towards two datasets to infer the
255 transcriptional impact of the timing of a mutation. From the TCGA-COAD cohort [21], we identified
256 48 samples which were $FBXW7^{mut}$ and 272 samples which were $FBXW7^{WT}$. We performed single-

257 sample gene set enrichment analysis (ssGSEA) on each of these samples against our FA_up gene
258 signature (Figure 6a). Intriguingly, we observed a negative association between our FA_up gene
259 signature (NES= -1.88, *p*-value= 2.22 x 10^{-7}), and a positive association between our FA_down gene
260 signature (NES= 2.10, *p*-value= 2.12 x 10^{-8}) in a comparison of *FBXW7*^{mut} vs *FBXW7*^{WT}. As we were
261 not able to determine when the acquisition of an *FBXW7* mutation occurred in cancers from the
262 TCGA-COAD cohort, we can only surmise that *FBXW7* mutations occurred when the cancer was
263 already at an advanced stage and therefore did not possess transcriptomic features in keeping with our
264 FA organoids. In addition, ssGSEA of samples showed there was an inverse relationship between our
265 FA_up and FA_down gene signatures (correlation score: -0.55, $p < 2.2 \times 10^{-16}$) (Figure 6b).
266 Reassuringly, this suggests that our FA_up gene signature represents a novel fetal regenerative/YAP
267 active geneset to identify cancer cells in this state.

268 We further analysed transcriptional data from the recently published EPICC dataset [10]. Here, the
269 authors had performed single-gland RNAseq on a number of phenotypically normal glands. We
270 analysed transcriptional data from phenotypically normal glands, and performed principal component
271 analysis (PCA) on these glands (Figure 6c). Notably, one gland had an *FBXW7* mutation in the
272 absence of an *APC* mutation, while another gland had an *APC* mutation in the absence of an *FBXW7*
273 mutation. Two glands possessed an *FBXW7* as well as an *APC* mutation, though it was not possible to
274 conclusively determine which mutation was acquired first. Intriguingly, the gland with an *APC*
275 mutation alone was located on the PCA diagram apart from all other glands. Notably, the two glands
276 which had both *APC* and *FBXW7* mutations also clustered closer to the wildtype and *FBXW7* mutant
277 gland, suggesting that these two glands could have acquired the *FBXW7* mutation prior to the *APC*
278 mutation, and therefore could explain why the glands still retained phenotypic normality. We
279 acknowledge that these inferences have been drawn based on a limited number of glands, but are
280 encouraged that existing patient-derived transcriptional data demonstrates concordance with our
281 findings.

282

283 Discussion

284 Recent work has uncovered that molecular background in intestinal tumours influences a complex
285 interplay between regenerative and homeostatic stem cell populations [19]. Whether similar
286 processes play a role in pre-neoplasia and how this changes temporally remain unexplored. Using
287 *FBXW7* as an exemplar, our analyses demonstrate that epigenetics underlie the context-specific
288 cellular response to somatic driver mutations, advancing the notion that tumour genotype alone does
289 not equate to phenotype.

290 In our study, we found introducing an *FBXW7* mutation in normal colon organoids generated little
291 transcriptional response and organoids remained broadly 'wildtype' although primed towards a
292 foetal/YAP-active state. These findings are compatible with the observation *in vivo* that *FBXW7*
293 mutations are found in histologically normal crypts but fails to explain why *FBXW7* mutations are
294 drivers in established CRC. In answer to this we found an epistatic effect of the mutation when
295 acquired on increasingly complex mutational backgrounds. Historically, epistatic phenomena have
296 been described in yeast biology and population genetics, but little explored in cancer due to
297 complexity in modelling.

298 Building on our demonstration of epistasis we tested whether simply re-ordering mutations generated
299 similar results. To our surprise not only were FA mutants distinct phenotypically from AF mutants but
300 transcriptionally they also remained near wildtype despite having lost two major tumour suppressor
301 genes. Mutational order effects have been described only once before in a *JAK2/TET2* mutant
302 haematological malignancy [22]. In a highly analogous manner, the authors found these blood
303 cancers with switched orders had alterations in stem cell hierarchies and transcriptional response.

304 To understand the link between mutation order, epistasis and stem cell hierarchies we tested whether
305 an epigenetic mechanism could underly our data. Chromatin accessibility analyses showed that whilst
306 both FA and AF organoids possessed more permissive chromatin than wildtype, broadly FA chromatin
307 was less accessible than AF accounting for the general repression in the transcriptional consequences
308 of an *APC* mutation. However, we found FA organoids did have increased accessibility to TEAD1
309 and TEAD2 motifs. These data explain the foetal/YAP active state seen with F and FA mutations.
310 Two very recent studies have explored chromatin landscapes in foetal and adult intestinal organoids

311 [23, 24]. In highly supportive findings, these studies show similar TEAD-family accessibility in foetal
312 organoids and *FBXW7* to be a top target in a CRISPR screen for regulators of the foetal intestinal
313 state. Ultimately, the mechanism by which *FBXW7* effects changes in chromatin accessibility remains
314 cryptic, though a similar observation has been observed previously [25]. Given FBXW7's important
315 role in the E3 ubiquitin ligase complex, we speculate that decreased substrate degradation of one or a
316 number of FBXW7 targets could result in this change in chromatin accessibility, though further work
317 to elucidate this mechanism will need to be performed.

318 Overall, our study explains the basis for why *FBXW7* mutations in normal colonic epithelia fail to
319 induce malignant transformation and provide the rationale for testing the translational impact of
320 mutational order across a wider mutational spectrum and different cancers.

321

322

323 Methods

324 Human material for organoid cultures

325 Ethics approval for the retrieval of human colon specimens was accorded by the University of Oxford
326 – Translation Gastroenterology Unit (16/YH/0247). Written consent was obtained from all patients.

327 Organoid culture

328 Colonic tissue was obtained from adult patients who were undergoing surgery for colorectal cancer. A
329 1 x 1 cm piece of colon from a region at least 5cm distant from the tumour, and appearing
330 phenotypically normal was resected. Organoids were derived based on a previously published
331 protocol [11]. Organoid culture growth media consists of advanced DMEM/F12 (Gibco), and
332 supplemented with penicillin/streptomycin (Gibco), 10mM HEPES buffer solution (Gibco), 2mM
333 GlutaMAX (Gibco), 50% Wnt3a conditioned medium (produced from ATCC CRL-2647 cell line),
334 25% R-spondin conditioned medium (produced from Cultrex HA-R-Spondin1-Fc 293T cells), 1X B-
335 27 plus supplement (Gibco), 10μM SB 202190 (Tocris), 0.5μM SB 431542 (Tocris), 1μM

336 prostaglandin E2 (Tocris), 50ng/ml Noggin (Peprotech), 50ng/ml EGF (Peprotech), 10mM
337 nicotinamide (Sigma-Aldrich), and 1.25mM N-acetylcysteine (Sigma-Aldrich). For selection of APC
338 mutants, Wnt3a and R-spondin conditioned media were withdrawn from the growth media for at least
339 3 weeks. For selection of TP53 mutants, growth media was supplemented with 10μM of Nutlin-3 for
340 at least 1 month (Sigma-Aldrich).

341 CRISPR/Cas9 gene editing of human organoids

342 sgRNAs were designed using Synthego's CRISPR Design Tool (Supplementary Table 1). For
343 *FBXW7*, a multiguide approach utilising three different guide RNAs in equal concentration was used.
344 This increased the targeting efficacy given the lack of a selecting agent which can be used to enrich
345 for *FBXW7* mutants. The AAVS1 site is a commonly used safe harbour locus which served as a
346 control to ensure studied effects were not a function of CRISPR gene editing.

347 Our protocol for gene editing human organoids has been described previously [11]. An
348 electroporation-based approach was used to maximise gene editing efficacy. Cells were first
349 dissociated into a single-cell suspension using TrypLe (Gibco) by incubating in a 37°C water bath for
350 10min. triturating at regular intervals. Organoids were then palleted with centrifugation at 400g for 6
351 min. Palleted organoids were resuspended in advanced DMEM, triturated and palleted by
352 centrifugation once more. A ribonucleoprotein (RNP) complex comprising Cas9 (Sigma-Aldrich) and
353 guide RNA in a molar ratio of 1:4 was resuspended in Buffer R (Invitrogen) and left to stand at room
354 temperature for 10min. Palleted organoids were resuspended in Buffer T (Invitrogen). The RNP
355 complex and resuspended organoids were then mixed. Electroporation was performed using a Neon
356 Transfection System (ThermoFisher) with the following settings – voltage 1350V, width 20ms, and
357 pulses 2. After electroporation, organoids are transferred into advanced DMEM and left to recover for
358 10min. Centrifugation was performed to pallet organoids, which were then resuspended in BME and
359 transferred to cell culture plates as described above. Following electroporation, organoids were
360 incubated for one week and allowed to expand. Primers which generated amplicons of approximately
361 500bp in length were designed on Benchling (Supplementary Table 1). Amplicons were Sanger
362 sequenced by an external vendor (Genewiz).

363 Protein lysates and western blot

364 Proteins were harvested using RIPA (ThermoFisher) with addition of protease and phosphatase
365 inhibitor cocktails (Sigma-Aldrich). Quantification of protein concentration was performed using
366 BCA assay (ThermoFisher).

367 For western blot, 30µg of protein was used for each lane. Proteins were separated using a NuPage 4 –
368 12% Bis-Tris gel (Invitrogen) and transferred onto a 0.45µm nitrocellulose membrane. For
369 phosphorylated proteins, 5% BSA was used. For non-phosphorylated proteins, 5% low-fat milk was
370 used. The membrane was blocked for 1 hour before overnight incubation with primary antibodies at
371 4°C. Rabbit anti-human FBXW7 antibody (1:2500, BS-8394R, Bioss, USA), rabbit anti-human
372 phosphor-CJUN antibody (1:2500, PA5-40193, Invitrogen, USA), rabbit anti-human CJUN antibody
373 (1:2500, ab40766, Abcam, USA), rabbit anti-human phosphor-CCNE1 antibody (1:2500, ab52195,
374 Abcam, USA), rabbit anti-human CCNE1 antibody (1:2500, ab33911, Abcam, USA), rabbit anti-
375 human phosphor-CMYC (1:2500, ab185655 and ab185656, Abcam, USA), rabbit anti-human CMYC
376 (1:2500, ab32072, Abcam, USA), rabbit anti-human NICD (1:2500, #4147, Cell signalling
377 technologies, USA), rabbit anti-human NOTCH1 (1:2500, ab52627, Abcam, USA), and rabbit anti-
378 human GAPDH (1:2500, ab52627, Abcam, USA) was used. The membrane was then incubated with
379 goat anti-rabbit antibody (1:5000, ab6721, Abcam, USA) at room temperature for 1 hour. The
380 membranes were then imaged with a ChemiDoc XRS+ system (Bio-Rad).

381 Immunofluorescence and imaging

382 IF for organoids was previously described in our protocol [11]. Briefly, media from the wells of
383 organoids was removed and fixation with 2% paraformaldehyde was performed. This was incubated
384 at room temperature for 30min. Organoids were then washed with ice-cold DPBS gently, and allowed
385 to settle by gravity. The supernatant was then removed, and blocked with Organoid Blocking Solution
386 comprising DPBS supplemented with 3% BSA, 1% Triton X-100, 1% saponin and 1% secondary
387 antibody animal serum. Blocking was performed for 3 hours at room temperature. Organoids were
388 again allowed to settle by gravity, and the supernatant was removed. Primary antibody diluted in

389 organoid blocking solution was then added to the organoids for 24 hours at 4°C. Organoids were then
390 washed with DPBS supplemented with 3% BSA, 1% Triton X-100, and 1% saponin. Secondary
391 antibody diluted in the organoid washing solution was then added to the organoids for 2 hours at 4°C.
392 After 2 hours, organoids were again washed with organoid washing solution. Phalloidin stain was
393 added to the organoids for 60min, before DAPI stain was added to the organoids for 5min. Imaging
394 was performed with the Andor Dragonfly High-Speed Confocal Microscope Systems (Oxford
395 Instruments). Antibodies used were mouse anti-human FBXW7 antibody (1:100, H00055294-M02.
396 Novus Biologicals, USA), goat anti-mouse IgG H&L (Dylight 550) (1:500, ab96872, Abcam, USA),
397 Phalloidin iFluor 647 (1:400, ab176759, Abcam, USA), and DAPI (300nM, D1306, Invitrogen, USA).

398 Co-culture of organoids

399 Transduction of organoids was performed to achieve stable expression of GFP or mCherry
400 fluorescence. Lentiviral particles were first generated by transfection of HEK293T cells with
401 pMDLg/pRRE, pRSV-Rev, pSF-CMV-VSVG (Sigma-Aldrich) and either pCDH-EF1-copGFP-T2A-
402 Puro for GFP fluorescence or pCDH-EF1-copGFP-T2A-Puro for mCherry fluorescence.
403 pMDLg/pRRE, and pRSV-Rev were gifts from Didier Trono (Addgene plasmid # 12251;
404 http://n2t.net/addgene:12251 ; RRID:Addgene_12251) [26], pCDH-EF1-copGFP-T2A-Puro and
405 pCDH-CMV-mCherry-T2A-Puro were gifts from Kazuhiro Oka (Addgene plasmid # 72263 ;
406 http://n2t.net/addgene:72263 ; RRID:Addgene_72263).

407 To transduce organoids with the lentivirus particle, the organoids were first dissociated into single-
408 cells by TrypLe for 10min in a 37°C water bath, with trituration at regular intervals. Single-cells were
409 centrifuged at 400g for 6 min to pallet cells, which were then passed through a 50μm filter. The
410 number of cells was then counted using a hemocytometer, and the required number of cells was
411 aspirated, centrifuged and then palleted. These cells were then resuspended in organoid growth media,
412 and viral particles were added to achieve a multiplicity of infection (MOI) of 20. Cells were infiltrated
413 over wells which had been overlaid with a pre-polymerised BME layer and left in a humidified 37°C
414 incubator for 24 hours. After 24 hours, dead cells were found floating above the BME, while live cells
415 would have become embedded in the BME. The media and dead cells were aspirated and fresh

organoid growth media was added. Fluorescence was checked using an EVOS M5000 cell imaging system (ThermoFisher) after 72 hours.

For the co-culture of organoids, a GFP-labelled population was co-cultured with an mCherry-labelled population in equal amounts to ascertain differences in proliferation. Cell culture wells were imaged on day 0, 1, 3, 5 and 7 using an EVOS M5000 cell imaging system (ThermoFisher). ImageJ was used to determine fluorescent intensity on each of these days.

Bulk RNA sequencing and analysis

Extraction of total RNA was performed using the RNeasy Mini Kit (Qiagen) as per manufacturer's protocol. The quantity and quality of the RNA was ascertained using the Agilent 2100 Bioanalyzer. Sequencing was performed by the Oxford Genomics Centre, Oxford using an Illumina NextSeq500 instrument using the standard paired-end protocol with a read length of 150bp. Fastq reads were processed to clip low quality leading and trailing edges and to remove any adapter content using Cutadapt (v.3.5). Quality checked FASTQ reads were aligned to the GRCh38 human genome and gene annotation (Ensembl release 105) using STAR aligner (v.2.7.3a) two-pass mode to generate gene-level quantification. Raw counts were processed in R (v.4.1.3) for all statistical testing and plotting purposes. Normalisation and differential expression were performed using limma (v.3.50.3). This included the generation of heatmaps using gplots (v.3.1.1) , volcano plots using ggplot2 (v3.3.5) and PCA plots using ggfortify (v.0.4.14). Gene set enrichment analysis was performed using fgsea (v.1.20.0) and GSVA (v.1.42.0).

Single-cell RNA sequencing and analysis

RNA extraction was performed as per bulk RNAseq. ScRNA-seq was conducted using a 5' scRNA-seq gene expression workflow (10x Genomics). Cells were loaded onto a 10x Chromium Controller for GEM generation followed by single cell library construction using 10x Chromium Next GEM Single Cell 5' Library and gel bead kit v1.1 following manufacturer's instructions. Size profiles of amplified cDNA and final libraries for sequencing were verified by electrophoresis (Agilent 2100 Bioanalyzer system, High Sensitivity DNA Kit), and the concentration of final libraries was measured

with Qubit (Thermo Fisher Scientific). Libraries were sequenced on an Illumina NextSeq 2000 (26 cycles read 1, 8 cycles i7 index, 98 cycles read 2), achieving a mean of 39,412 reads per cell. Gene by cell barcode quantification matrix were obtained using Cell Ranger (v.7.0.1) and Seurat (v.4.2.0) was used to perform normalisation and UMAP based cluster assignment of pass cells. Single sample gene set enrichment analyses (ssgsea) method from GSVA (v.1.42.0) was used on a custom list of gene signature sets defined by editing the MSigDb (v.7.5.1) pathways to leave out SPERMATOGENSIS, MYOGENESIS and PANCREAS_BETA_CELLS, and replacing the default WNT_BETA_CATENIN_SIGNALING set by WNT_SIGNALING gene set (MSigDb systematic name M5493), as per Household et al. [27]. Additional gene sets included were – genes up- or down-regulated in bulk RNA-seq comparison of 'FBXW7-APC' versus 'APC-FBXW7' organoids (adjusted p-value < 0.05 and logFC >= |1.5|; n= 248 up- and n= 166 down-regulated genes), mouse foetal gastric epithelium gene set from Vallone et al. 2016 (n= 122 human homologues), intestinal stem cell signature from Merlos-Suárez et al. 2011 (n= 74), YAP pathway signature from Gregorieff et al. 2015 (n= 213 human homologues), crypt-base columnar (CBC) and regenerative stem cell (RSC) signature sets from Vazquez et al. 2022 (n= 340 and 206 human homologues respectively)(Supplementary table 3). Enrichment scores obtained per gene set was z-score transformed, and cells with scores greater than 3rd quartile or less than 1st quartile of the score distribution were termed as enriched or depleted respectively, for that gene set. To assess statistical enrichment or depletion of a given gene set in FBXW7 mutant versus wildtype categories, chi-square test was applied on contingency table for cell counts from enriched or depleted classes. Pearson residuals were visualised using mosaic plot from R package vcd (v.1.4-11). For RNA velocity analysis, separate count matrices for spliced and unspliced transcripts were created using Kallisto-Bustools (v.0.27.3) with the La Manno et al. 2018 strategy, while using the same reference annotation from Cell Ranger (GRCh38, v.2020-A). Spliced/ unspliced count data were combined with Seurat based UMAP clustering using scVelo (v.0.2.5) under python v.3.10.6. RNA velocity graph computed was overlaid on UMAP cluster embeddings to infer trajectory direction.

Assay for transposase-accessible chromatin sequencing (ATACseq) and analysis

469 Library preparation for ATACseq was performed using the ATAC-Seq Kit (Active Motif) as per the
470 manufacturer's instructions. Multiplexing was performed using unique i7 and i5 indexed primers. The
471 quantity and quality of DNA was assessed using the Agilent High Sensitivity DNA Kit, ensuring that
472 transposed DNA fragments were between 200 and 1000bp, with a periodicity of ~200bp. Sequencing
473 was performed by the Oxford Genomics Centre, Oxford using an Illumina NextSeq2000 instrument.
474 Quality checked fastq reads were aligned to the human genome (GRCh38) using bwa aligner
475 (v.0.7.17). Alignment output (BAM files) were filtered, and TA (Tag Alignment) format data created
476 using samtools (v.1.14), picard (v.2.6.0) and bedtools (v.2.30.0). Further, MACS3 (v.3.0.0b2) was
477 used to perform peak calling which were then annotated using ChIPseeker (v.1.30.3). MACS3
478 identified peaks for the 'AF vs W' and 'FA vs W' comparisons were thresholded to select those with
479 score (i.e., -10*log(q-value)) >median of the respective distribution, overlapping regions merged and
480 the 50bp span from the centre of the peak region were extracted as input for *de novo* transcription
481 factor motif enrichment analysis using rGADEM (v.2.46.0). Identified motifs were plotted using
482 TFBSTools (v.1.36.0) and annotated for the closest matching core human transcription factors using
483 JASPAR2020 (v.0.99.0). Gene/ motif-set level visualisation of ATAC-seq signal enrichment was
484 performed using deeptools (v.3.5.2). Comparative bigwig files were created for 'AF vs W', 'FA vs W'
485 and 'FA vs AF' with BPM (Bins per million) normalisation, non-covered regions skipped, ENCODE
486 blacklist regions filtered out and effective genome size adjusted to reflect the filtering. The bigwig
487 files were then profiled for ATAC-seq signal enrichment with reference-point at the TSS
488 (Transcription Start Site) and upstream/ downstream 5kb region. Signal enrichments were profiled for
489 each of these sets –all genes in the genome (gencode v.38; 'Whole Genome'), the CBC gene signature
490 set ('CBC') and the 50bp genomic regions where de novo motif search identified TEAD1/2 motifs
491 (542 regions; 'TEAD1/2 motif') or, SNAI1 motifs (491 regions; 'SNAI1 motif').

492 Validation of results in published datasets

493 Two independent and published datasets were used to validate our findings. Somatic mutation and
494 gene expression for the TCGA-COAD cohort were obtained from NCI-GDC data portal [21], to
495 create a dataset of colon adenocarcinoma cases only from 320 unique patients of whom 48 were

496 mutated and remaining wild-type for FBXW7. Differential gene-expression between *FBXW7*$^{mut.}$ and
497 *FBXW7*^{WT} samples was performed and the GSEA score for the FA up- and down-regulated gene sets
498 was evaluated using fgsea (v.1.20.0). Per-sample enrichment scores for the gene sets was calculated
499 using 'ssgsea' method in GSVA (v.1.42.0). The second validation made use of transcriptomic results
500 derived from the EPICC dataset [10]. Here, individual gland-level transcriptomic results were
501 obtained. Generation of heatmaps was performed using gplots (v.3.1.1) and PCA plots using ggplot2
502 (v3.3.5).

503 Acknowledgements

504 S.J.A.B. was supported by The Pharsalia Trust, UK & Cancer Research UK Advanced Clinician
505 Scientist Fellowship (C14094/A27178). D.K.H.C. was supported by Singapore Ministry of Health's
506 National Medical Research Council under a research training fellowship (MOH-FLWSHP10may-
507 0001).

508 Author contributions

509 D.K.H.C. performed the experiments and wrote the initial draft of the manuscript, and was supervised
510 by S.J.A.B. A.M. performed bioinformatic analysis for the project. S.D.C. assisted with
511 immunofluorescence of organoids. Y. Z. assisted with generation of plasmids for lentiviral labelling of
512 organoids. R.O. and X.L. assisted with scRNAseq. J.H. and T.G. contributed the EPICC dataset and
513 assisted with its analysis. S.J.A.B. was overall in-charge of the project. All authors contributed to
514 drafting and final approval of the manuscript.

515 Competing interests

516 The authors declare no competing interests.

517 Materials and correspondence

518 Raw sequence data would be made available via the European Genome-Phenome Archive (EGA), on
519 publication of the manuscript. Please relay correspondence to Simon Buczacki.

520 Inclusion and ethics in global research

Research was conducted in accordance with principles of inclusion and good ethics in global research.

Code availability

All relevant scripts to replicate the analysis would be made available on Github on publication of the manuscript

542 References

543 1. Brunner, S.F., et al., *Somatic mutations and clonal dynamics in healthy and cirrhotic human*
544 *liver.* Nature, 2019. **574**(7779): p. 538-542.
545 2. Colom, B., et al., *Spatial competition shapes the dynamic mutational landscape of normal*
546 *esophageal epithelium.* Nat Genet, 2020. **52**(6): p. 604-614.
547 3. Martincorena, I., et al., *Tumor evolution. High burden and pervasive positive selection of*
548 *somatic mutations in normal human skin.* Science, 2015. **348**(6237): p. 880-6.
549 4. Moore, L., et al., *The mutational landscape of normal human endometrial epithelium.* Nature,
550 2020. **580**(7805): p. 640-646.
551 5. Lee-Six, H., et al., *The landscape of somatic mutation in normal colorectal epithelial cells.*
552 Nature, 2019. **574**(7779): p. 532-537.
553 6. Ng, A.S. and D.K.H. Chan, *Commonalities and differences in the mutational signature and*
554 *somatic driver mutation landscape across solid and hollow viscus organs.* Oncogene, 2023.
555 7. Yeh, C.H., M. Bellon, and C. Nicot, *FBXW7: a critical tumor suppressor of human cancers.*
556 Mol Cancer, 2018. **17**(1): p. 115.
557 8. Burdziak, C., et al., *Epigenetic plasticity cooperates with cell-cell interactions to direct*
558 *pancreatic tumorigenesis.* Science, 2023. **380**(6645): p. eadd5327.
559 9. Johnstone, S.E., et al., *Large-Scale Topological Changes Restrain Malignant Progression in*
560 *Colorectal Cancer.* Cell, 2020. **182**(6): p. 1474-1489.e23.
561 10. Heide, T., et al., *The co-evolution of the genome and epigenome in colorectal cancer.* Nature,
562 2022. **611**(7937): p. 733-743.
563 11. Chan, D.K.H., S.D. Collins, and S.J.A. Buczacki, *Generation and immunofluorescent*
564 *validation of gene knockouts in adult human colonic organoids using multi-guide RNA*
565 *CRISPR-Cas9.* STAR Protoc, 2023. **4**(1): p. 101978.
566 12. Chan, D.K.H., et al., *Biallelic FBXW7 knockout induces AKAP8-mediated DNA damage in*
567 *neighbouring wildtype cells.* Cell Death Discov, 2023. **9**(1): p. 200.

568 13. van Neerven, S.M., et al., *Apc-mutant cells act as supercompetitors in intestinal tumour*
569 *initiation.* Nature, 2021. **594**(7863): p. 436-441.
570 14. Drost, J., et al., *Sequential cancer mutations in cultured human intestinal stem cells.* Nature,
571 2015. **521**(7550): p. 43-7.
572 15. Matano, M., et al., *Modeling colorectal cancer using CRISPR-Cas9-mediated engineering of*
573 *human intestinal organoids.* Nat Med, 2015. **21**(3): p. 256-62.
574 16. Fernandez Vallone, V., et al., *Trop2 marks transient gastric fetal epithelium and adult*
575 *regenerating cells after epithelial damage.* Development, 2016. **143**(9): p. 1452-63.
576 17. Gregorieff, A., et al., *Yap-dependent reprogramming of Lgr5(+) stem cells drives intestinal*
577 *regeneration and cancer.* Nature, 2015. **526**(7575): p. 715-8.
578 18. Merlos-Suárez, A., et al., *The intestinal stem cell signature identifies colorectal cancer stem*
579 *cells and predicts disease relapse.* Cell Stem Cell, 2011. **8**(5): p. 511-24.
580 19. Vasquez, E.G., et al., *Dynamic and adaptive cancer stem cell population admixture in*
581 *colorectal neoplasia.* Cell Stem Cell, 2022. **29**(8): p. 1213-1228.e8.
582 20. Lin, K.C., H.W. Park, and K.L. Guan, *Regulation of the Hippo Pathway Transcription Factor*
583 *TEAD.* Trends Biochem Sci, 2017. **42**(11): p. 862-872.
584 21. *TCGA-COAD*. 7 March 2023]; Available from: https://portal.gdc.cancer.gov/projects/TCGA-
585 COAD.
586 22. Ortmann, C.A., et al., *Effect of mutation order on myeloproliferative neoplasms.* N Engl J
587 Med, 2015. **372**(7): p. 601-612.
588 23. Hansen, S.L., et al., *An organoid-based CRISPR-Cas9 screen for regulators of intestinal*
589 *epithelial maturation and cell fate.* Sci Adv, 2023. **9**(28): p. eadg4055.
590 24. Pikkupeura, L.M., et al., *Transcriptional and epigenomic profiling identifies YAP signaling as*
591 *a key regulator of intestinal epithelium maturation.* Sci Adv, 2023. **9**(28): p. eadf9460.
592 25. Thirimanne, H.N., et al., *Global and context-specific transcriptional consequences of*
593 *oncogenic Fbw7 mutations.* Elife, 2022. **11**.
594 26. Dull, T., et al., *A third-generation lentivirus vector with a conditional packaging system.* J
595 Virol, 1998. **72**(11): p. 8463-71.

27. Household, J., et al., *Phenotypic plasticity and genetic control in colorectal cancer evolution.* Nature, 2022. **611**(7937): p. 744-753.

617 Figure legends

618 Figure 1: Characterisation of W and F organoids. a. Brightfield microscopy of W and F organoids
619 revealed no observable phenotypic differences. Scale bars represent 500µm. b. Western blot validation
620 showing loss of FBXW7 protein in F organoids. c. Immunofluorescence of W and F organoids with
621 DAPI nuclear stain (blue), F-actin (red), FBXW7 (orange). Scale bars represent 100µm. d. FBXW7
622 targets the phosphorylated substrates and ubiquitinates these substrates for proteasomal degradation.
623 This included phosphorylated cJun, phosphorylated CCNE1, phosphosylated cMyc, and notch
624 intracellular domain (NICD). The non-phosphorylated substrates were affected to varying degrees.
625 While upregulation of cJun, was observed, there was no change in the quantities of CCNE1, cMYC
626 and NOTCH. e. Volcano plot from bulk RNAseq of F vs W organoids revealed minimal differential
627 expression of genes. Only *HLA-DQB1* was found to be significantly downregulated, and *GSTM1*
628 significantly upregulated in F organoids. All experiments were performed with N = 3 biological
629 replicates.

630 Figure 2: Effect of *FBXW7* mutation is dependent on the mutational background. a. Schematic
631 showing the organoid models used in this analysis. W, A and AT organoids were generated to reflect
632 normal, adenomatous and carcinomatous lesions. On each of these organoid types, an *FBXW7*
633 mutation was introduced to generate F, AF and ATF organoids respectively. b. Brightfield microscope
634 of A, AF, AT and ATF organoids. A organoids adopt a cystic phenotype which is representative of
635 increased proliferation. AF organoids appear smaller in size compared with A organoids. AT organoids
636 also recapitulate the cystic appearance of A organoids. ATF organoids appear less cystic than AT
637 organoids. c. The number of differentially expressed genes on the addition of an *FBXW7* mutation
638 changes based on the mutational background. While 2 genes were differentially expressed between W
639 and F, 87 and 294 genes were differentially expressed between A and AF, and AT and ATF
640 respectively. d. Hierarchical clustering of the different organoid types showed that W and F organoids
641 clustered most similarly together. All experiments were performed with N = 3 biological replicates.

642 Figure 3: Effect of *FBXW7* mutation is dependent on the order of mutation. a. Schematic showing the
643 organoid models used in this analysis. A and F organoids were generated separately. On the A

644 organoid, an *FBXW7* mutation was introduced, generating AF organoids. On the F organoid, an *APC*
645 mutation was introduced, generating FA organoids. AF and FA organoids possessed the same
646 mutations but acquired the mutations in an inverse order. b. Brightfield microscope of A, AF, F and
647 FA organoids. Although FA organoids acquired an *APC* mutation, this did not recapitulate the cystic
648 phenotype observed in A or AF organoids. c. Principle-component analysis (PCA) showed not only
649 that FA organoids clustered separately from AF organoids, FA organoids clustered together with W
650 and F organoids, while AF organoids clustered closer to A organoids. d. Venn diagram depicting the
651 overlap of differentially expressed genes at cut-off log2FC $\leqslant$ -0.7 or $\geqslant$ 0.7 between AF vs W and FA
652 vs W comparisons. 628 genes were differentially expressed in both AF and FA organoids. e. Analysis
653 of these 628 genes showed there was a reduction in the magnitude by which the genes were
654 differentially expressed, suggesting a dampening effect of changing the order of mutation on the
655 transcriptome. All experiments were performed with N = 3 biological replicates.

656 Figure 4: scRNAseq of W and F organoids demonstrated differences on gene signature and pathway
657 analysis. a. Uniform manifold approximation and projection (UMAP) analysis from scRNAseq of W
658 and F organoids yielded 14 clusters. b. Cluster 13 was unique to F organoids. c. *FBXW7* is actively
659 expressed in wildtype organoids. d. RNA velocity analysis demonstrated that clusters 1, 8 and 13 were
660 terminally differentiating subpopulations. Chi-square analysis of W and F organoids demonstrated
661 that F organoids were enriched for (e) FA_up gene signature ($p < 2.22 \times 10^{-16}$), (f) fetal signature ($p =$
662 9.4754×10^{-11}), (g) YAP pathway signature ($p = 3.2134 \times 10^{-7}$), and depleted for (h) intestinal stem cell
663 signature ($p = 1.4887 \times 10^{-6}$) and (i) crypt-based columnar stem cell signature ($p < 2.22 \times 10^{-16}$). All
664 experiments were performed with N = 3 biological replicates.

665 Figure 5: ATACseq analysis suggested cell state changes are due to alterations in chromatin
666 accessibility. a. Chromatin accessibility of the whole genome was decreased in FA vs W organoids
667 compared with AF vs W organoids, which could account for the dampened transcriptional impact of
668 FA vs AF organoids. b. Chromatin accessibility of CBC signature genes was increased in AF vs W
669 organoids compared with FA vs W organoids, in concordance with expression of the CBC signature
670 observed on scRNAseq. Motif plots of the two *de novo* motifs found enriched in the FA vs W

organoid comparison were (c) “nCwGCmCwGn” and (d) "rGCAGGTGn”. Chromatin accessibility of TEAD1/2 (e) and SNAI1 (f) motifs were upregulated in FA vs W organoids compared with AF vs W organoids. All experiments were performed with N = 3 biological replicates.

Figure 6: Validation of results in patient data. a. Using TCGA-COAD data, single-sample gene set enrichment analysis (ssGSEA) of 48 samples which were *FBXW7*^{Mut} and 272 samples which were *FBXW7*^{WT} demonstrated a negative association with the FA_up gene set, and a positive association with the FA_down gene set in a comparison between *FBXW7*^{Mut} and *FBXW7*^{WT}. b. Moreover, there was an inverse relationship between the enrichment score for the FA up- and down-regulated gene sets (derived from FA vs AF organoids) across the 320 samples in the TCGA-COAD (correlation score: -0.55, $p < 2.2 \times 10^{-16}$). Together, these suggest that our FA_up gene signature represents a novel fetal regenerative/YAP active geneset to identify cells in this state. c. PCA of phenotypically normal intestinal glands from a recently published EPICC dataset [10] showed that a gland with both an *APC* and *FBXW7* mutation clustered closer to the *FBXW7*-mutant gland and apart from the *APC* gland, which could account for its phenotypic appearance.

Extended data figure 1: *FBXW7*$^{-/-}$ organoids do not influence growth of neighbouring wildtype organoids. *APC*$^{-/-}$ cells act as supercompetitors which suppress the growth of neighbouring wildtype cells, evidenced by proliferative advantage of A organoids over neighboring W organoids (a, c, d). A similar effect was not seen in F organoids co-cultured with W organoids (b, e, f). g. EdU assay for W and F organoids showed no significant differences in proliferation rate. Volcano plot of co-cultured W versus non-co-cultured W (h) and co-cultured F versus non-co-cultured F (i) organoids showed that the effect of co-culture did not significantly influence the transcriptome. The values in this figure are mean ± sd, and statistical significance was measured by unpaired t-test. All experiments were performed with N = 3 biological replicates.

Extended data figure 2: Mutational background influences the transcriptomic effect of an *FBXW7* mutation. a. Volcano plot of AF vs A organoids. b. Volcano plot of ATF vs AT organoids. All experiments were performed with N = 3 biological replicates.

697 Extended data figure 3: Effect of epistasis not an artefact of CRISPR/Cas9 gene editing. a. Brightfield
698 microscopy of organoids which had been gene edited at the AAVS1 loci three times to mimic triple-
699 mutant ATF organoids. AAVS1 organoids did not adopt a cystic phenotype. b. Volcano plot of AAVS1
700 vs W organoids. c. Volcano plot of ATF vs W organoids. All experiments were performed with N = 3
701 biological replicates.

702 Extended data figure 4: Cluster 13 in F organoids was marked by EMT signature.

703 Extended data figure 5: GSEA of bulk RNAseq data of F vs W organoids using key pathways derived
704 from scRNAseq analysis. There was a significant upregulation of the fetal signature [16] (a), and YAP
705 pathway (b) in F organoids compared with W organoids. There was a negative association in ISC (c)
706 and CBC (d) signatures though this did not reach statistical significance. We however observed that
707 our FA gene set was negatively correlated in F organoids (e).

708 Extended data figure 6: GSEA of bulk RNAseq data of FA vs W and AF vs W for the YAP pathway
709 signature. There was a stronger association between a. FA vs W organoids, than b. AF vs W organoids
710 for the YAP pathway signature.

711 Supplementary Table 1: Guide RNA sequences for CRISPR/Cas9 gene editing with primer sequences
712 for validation

713 Supplementary Table 2: Comparison of differentially expressed genes from all bulk RNAseq
714 experiments

715 Supplementary Table 3: Gene sets

a

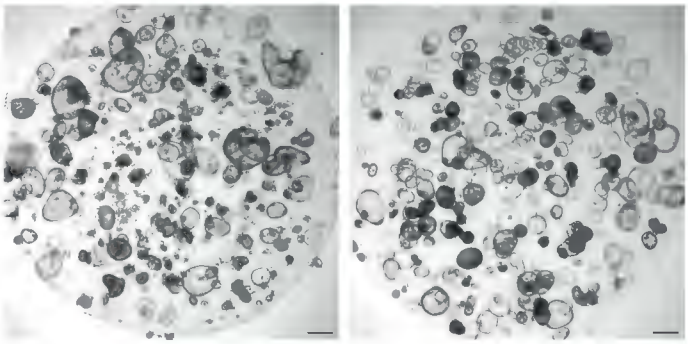
WT
FBXW7 -/-

b

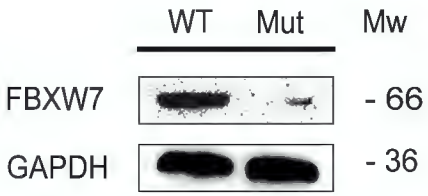
WT
Mut
Mw
FBXW7
- 66
GAPDH
- 36

c

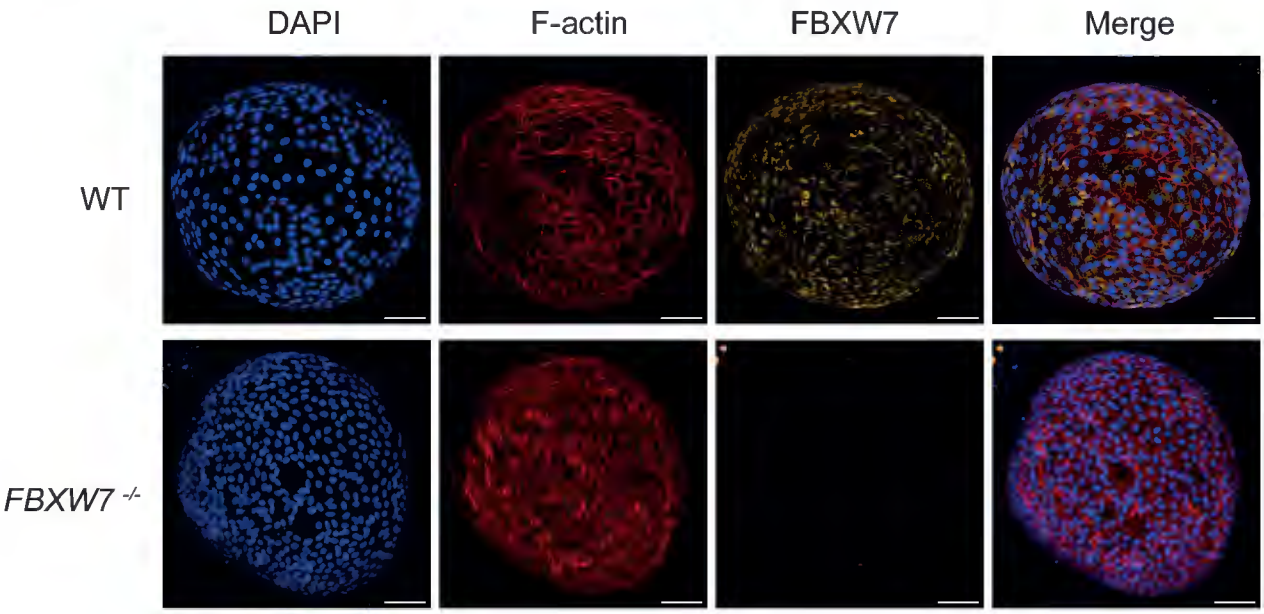
DAPI
F-actin
FBXW7
Merge
WT
FBXW7 -/-

d

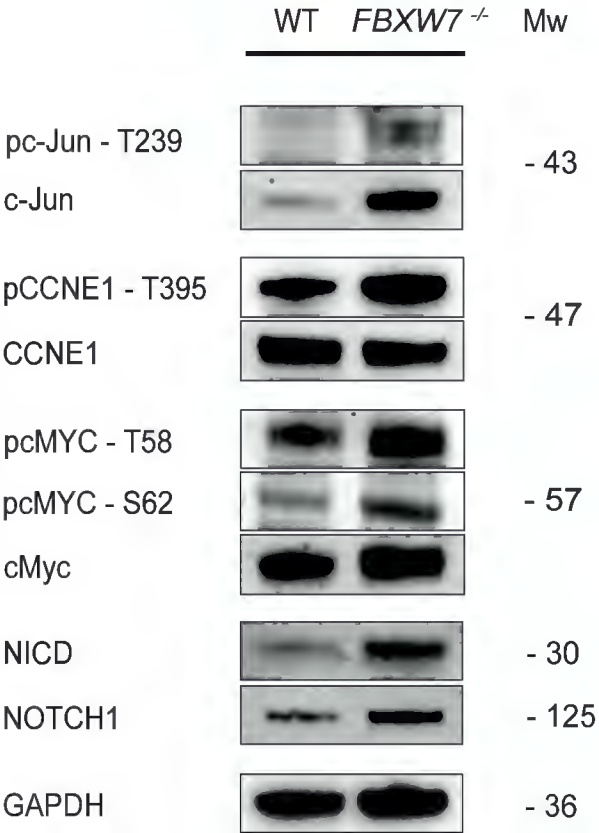
WT
FBXW7 -/-
Mw
pc-Jun - T239
c-Jun
- 43
pCCNE1 - T395
CCNE1
- 47
pcMYC - T58
pcMYC - S62
cMyc
- 57
NICD
NOTCH1
- 30
- 125
GAPDH
- 36

e

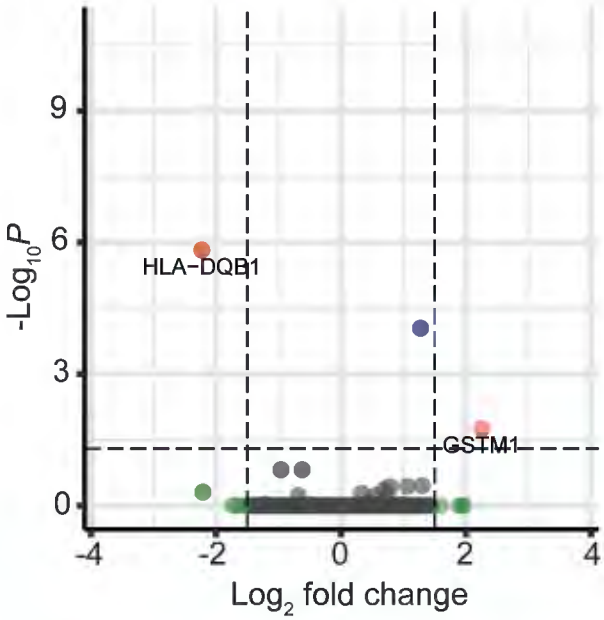
-Log10P
9
6
3
0
HLA-DQB1
GSTM1
-4
-2
0
2
4
Log2 fold change

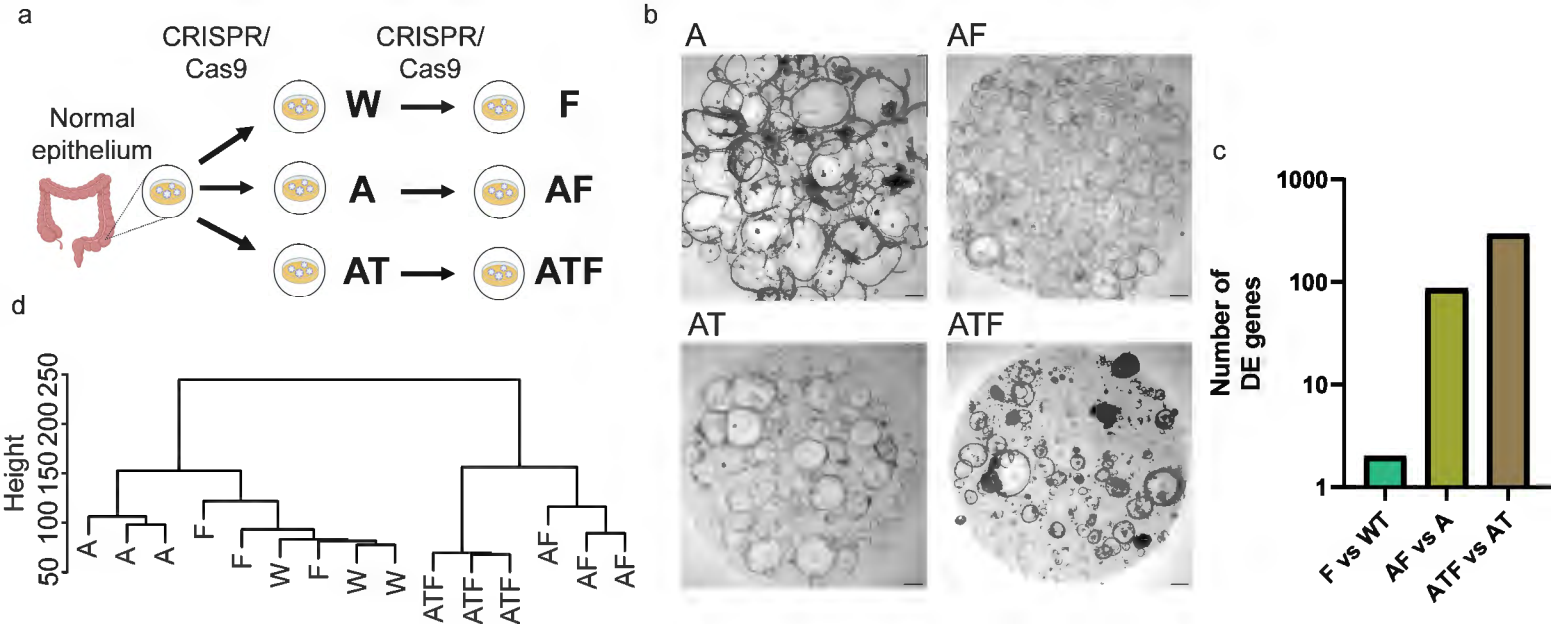
a
CRISPR/
Cas9
CRISPR/
Cas9
Normal
epithelium
W
F
A
AF
AT
ATF
b
A
AF
AT
ATF
c
Number of
DE genes
1000
100
10
1
F vs WT
AF vs A
ATF vs AT
d
Height
50 100 150 200 250
A
A
A
F
F
W
F
W
W
ATF
ATF
ATF
AF
AF
AF

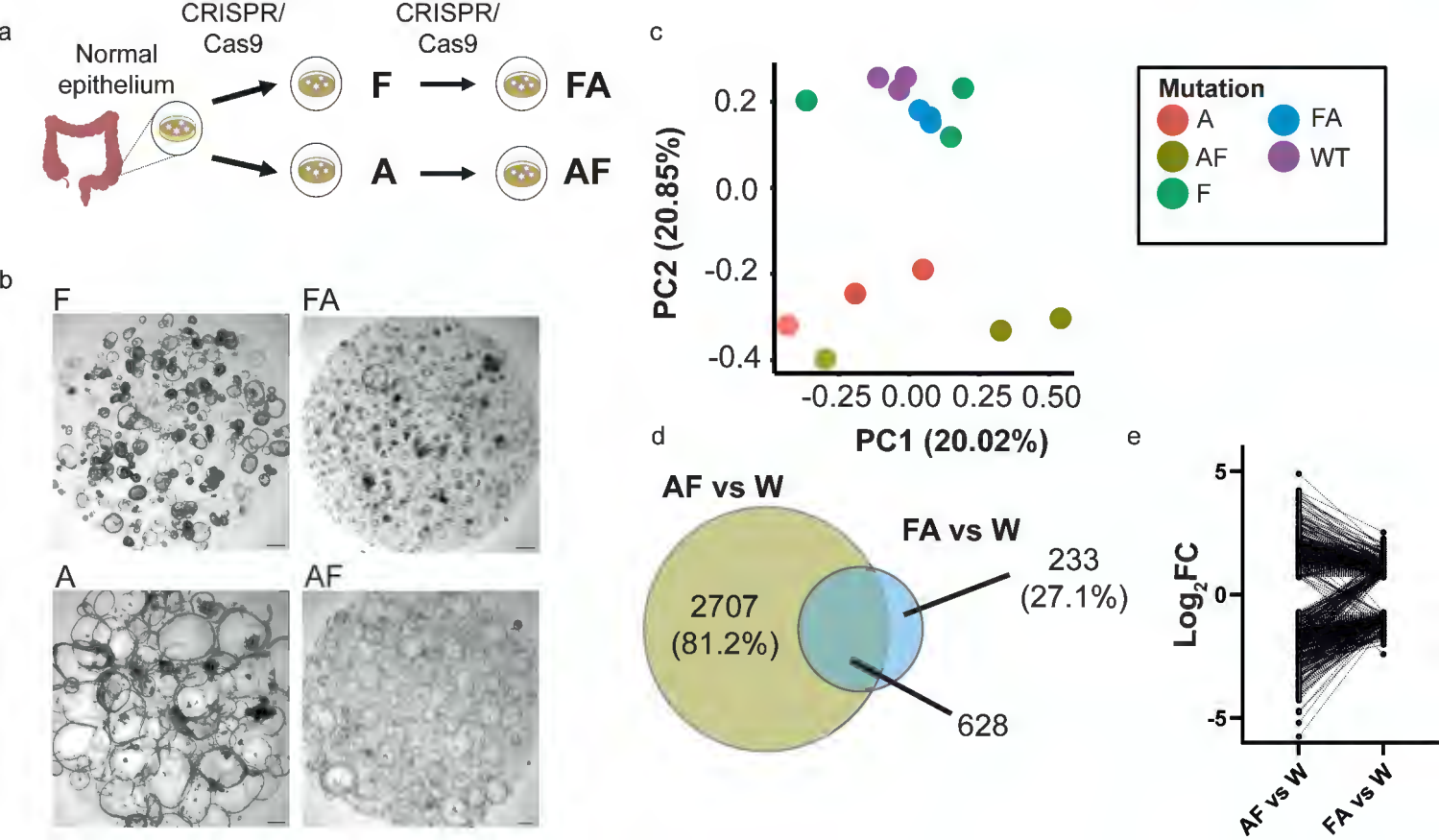
a
Normal epithelium
CRISPR/ Cas9
CRISPR/ Cas9
F
FA
A
AF
b
F
FA
A
AF
c
Mutation
A
FA
AF
WT
F
PC2 (20.85%)
PC1 (20.02%)
0.2
0.0
-0.2
-0.4
-0.25 0.00 0.25 0.50
d
AF vs W
FA vs W
2707 (81.2%)
233 (27.1%)
628
e
Log2FC
5
0
-5
AF vs W
FA vs W

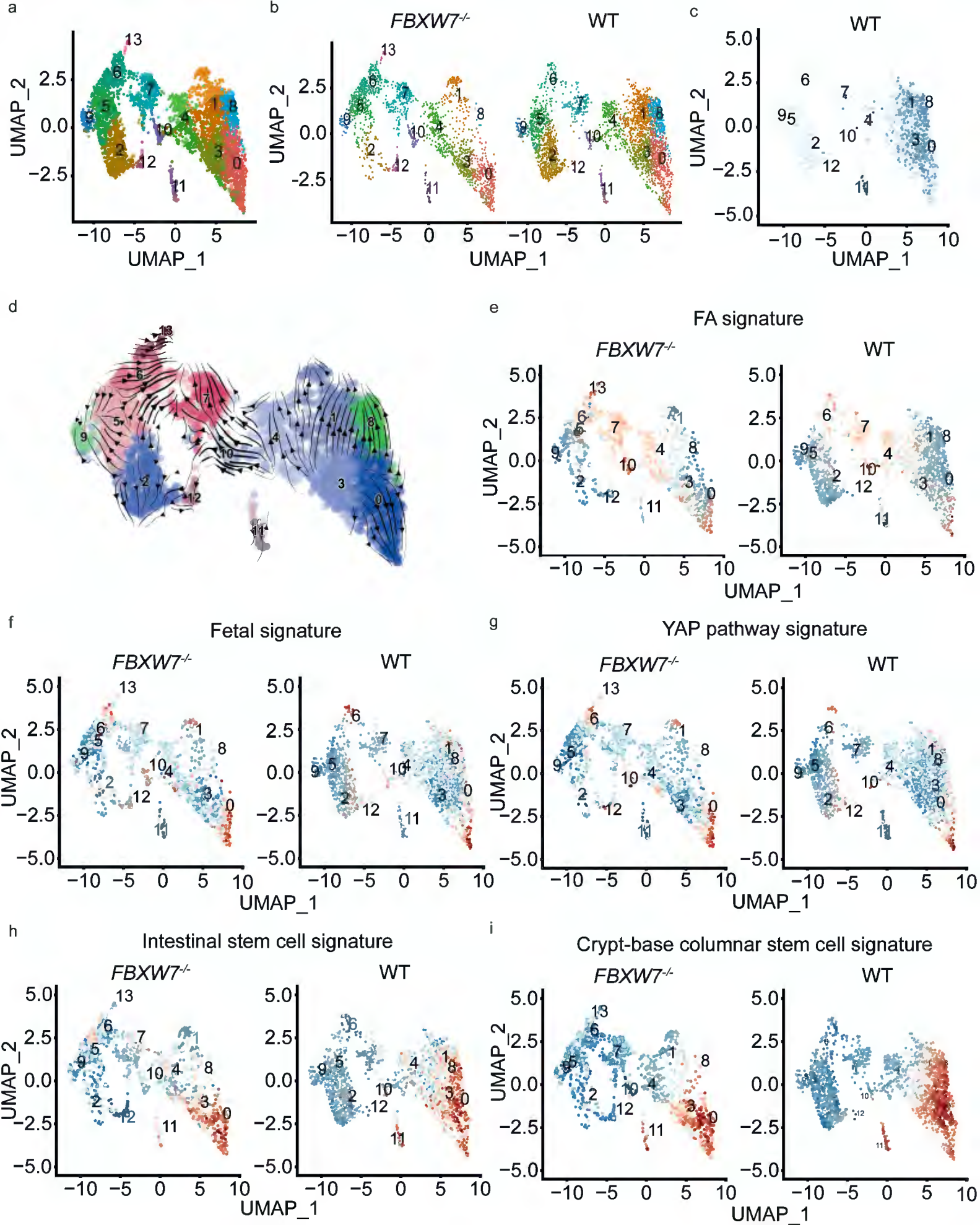
a
b
c
d
e
f
g
h
i
FBXW7-/-
WT
FA signature
Fetal signature
YAP pathway signature
Intestinal stem cell signature
Crypt-base columnar stem cell signature
UMAP_1
UMAP_2

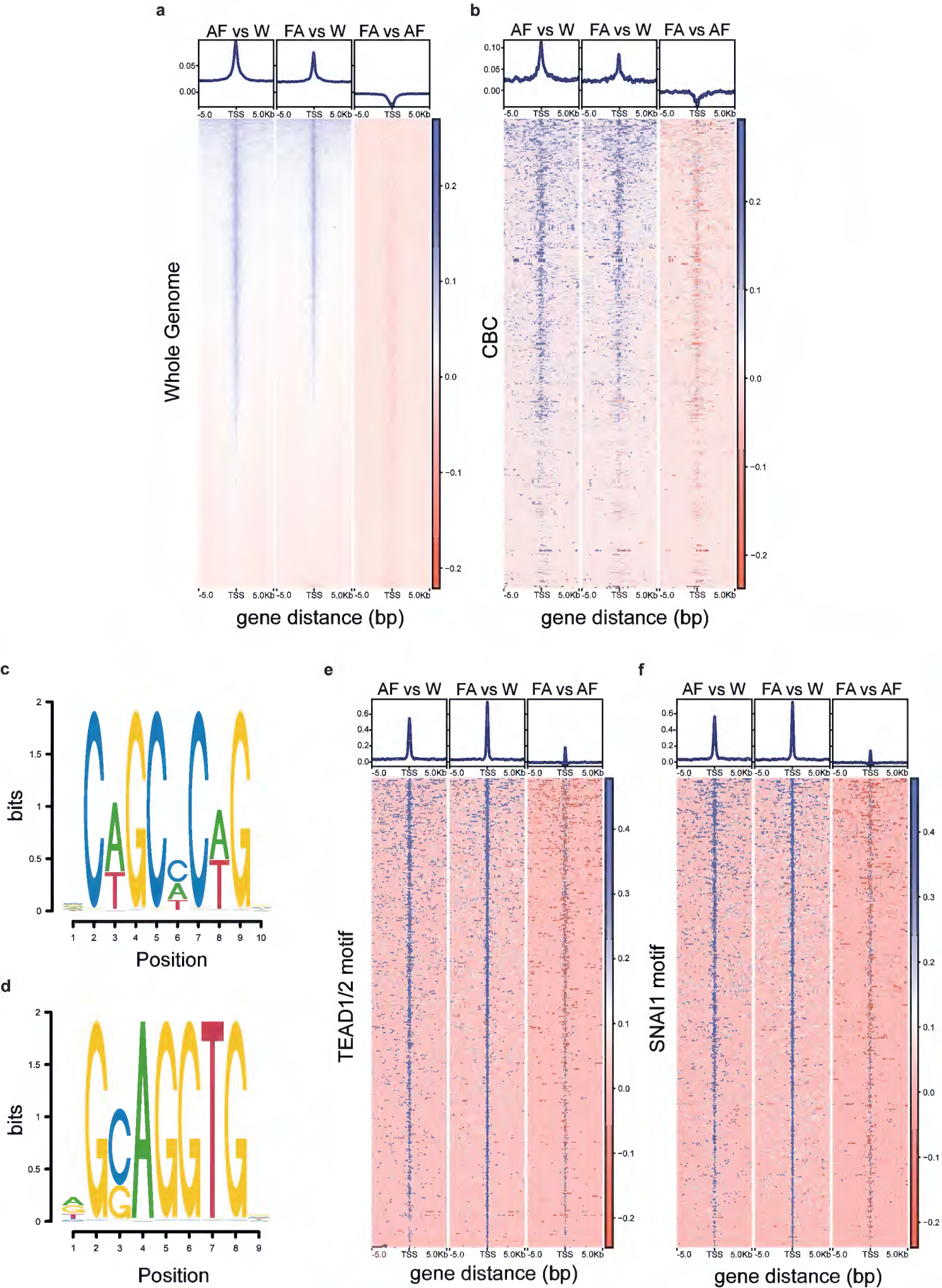
a
AF vs W
FA vs W
FA vs AF
Whole Genome
gene distance (bp)
b
CBC
gene distance (bp)
c
bits
Position
d
bits
Position
e
TEAD1/2 motif
gene distance (bp)
f
SNAI1 motif
gene distance (bp)
-5.0
TSS
5.0Kb

a

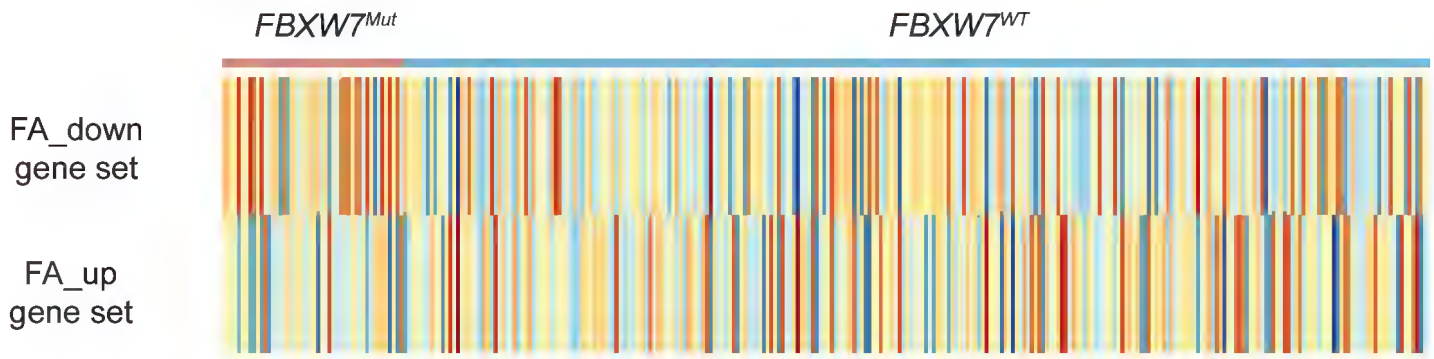
FBXW7Mut
FBXW7WT
FA_down gene set
FA_up gene set

b

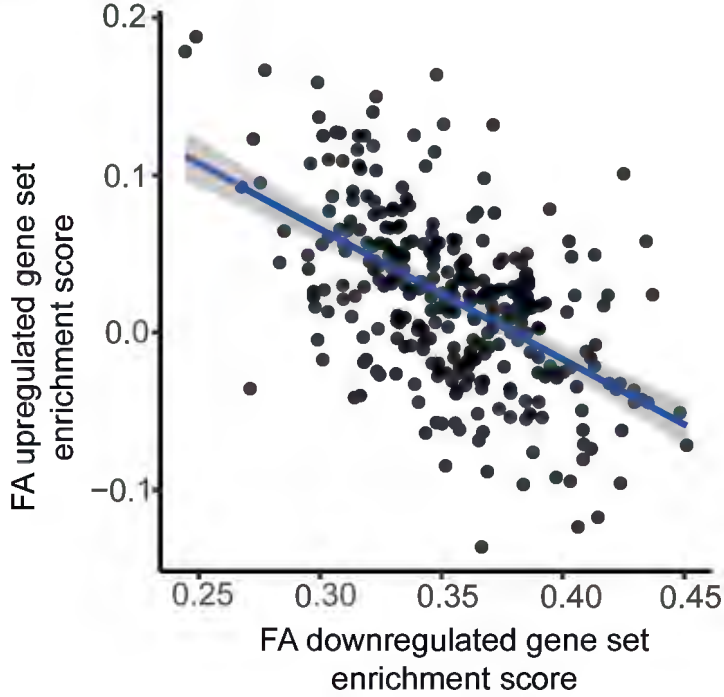
0.2
0.1
0.0
−0.1
FA upregulated gene set enrichment score
0.25
0.30
0.35
0.40
0.45
FA downregulated gene set enrichment score

c

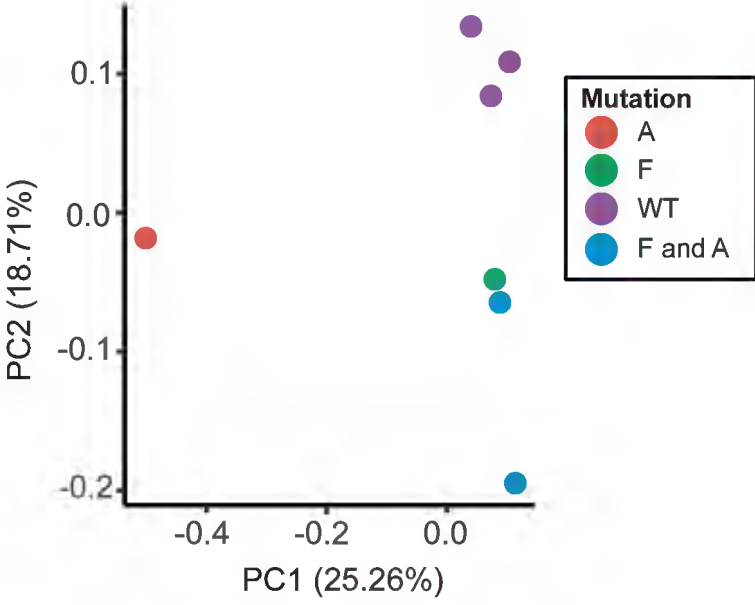
0.1
0.0
-0.1
-0.2
PC2 (18.71%)
-0.4
-0.2
0.0
PC1 (25.26%)
Mutation
A
F
WT
F and A

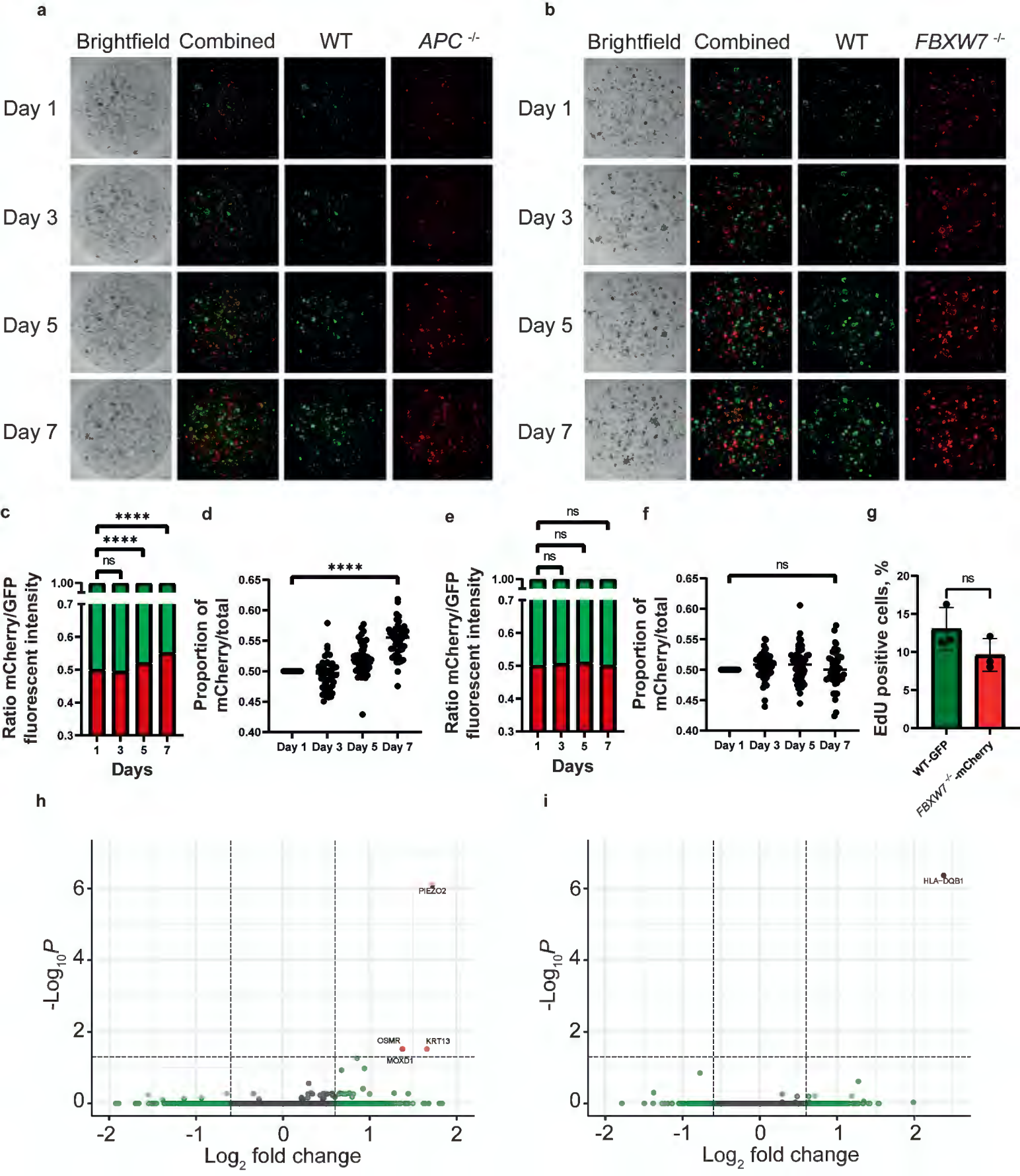
a
Brightfield
Combined
WT
APC -/-
Day 1
Day 3
Day 5
Day 7
b
Brightfield
Combined
WT
FBXW7 -/-
Day 1
Day 3
Day 5
Day 7
c
****
****
ns
Ratio mCherry/GFP fluorescent intensity
Days
d
****
Proportion of mCherry/total
Day 1 Day 3 Day 5 Day 7
e
ns
ns
ns
Ratio mCherry/GFP fluorescent intensity
Days
f
ns
Proportion of mCherry/total
Day 1 Day 3 Day 5 Day 7
g
ns
EdU positive cells, %
WT-GFP
FBXW7 -/- -mCherry
h
PIEZO2
OSMR
KRT13
MOXD1
-Log10P
Log2 fold change
i
HLA-DQB1
-Log10P
Log2 fold change

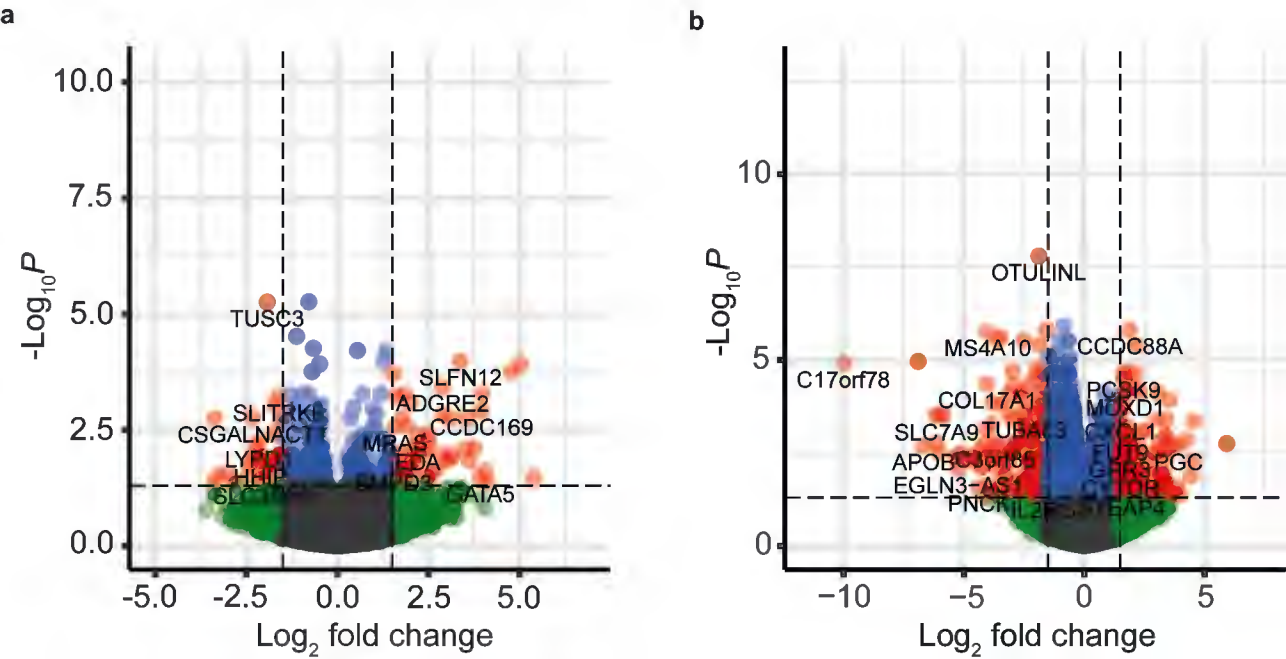
a
10.0
7.5
5.0
2.5
0.0
-Log10P
TUSC3
SLFN12
ADGRE2
CCDC169
MRAS
EDA
GATA5
-5.0
-2.5
0.0
2.5
5.0
Log2 fold change
b
10
5
0
-Log10P
OTULINL
MS4A10
CCDC88A
C17orf78
COL17A1
PCSK9
MOXD1
SLC7A9
TUBA
CXCL1
APOB
C3orf85
PGC
EGLN3-AS1
PNCK
EAP4
−10
−5
0
5
Log2 fold change

a

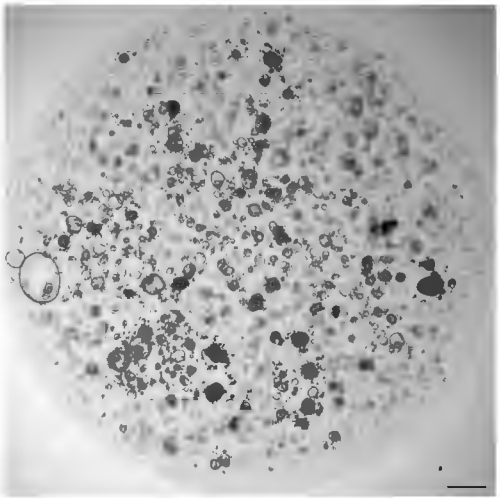

b

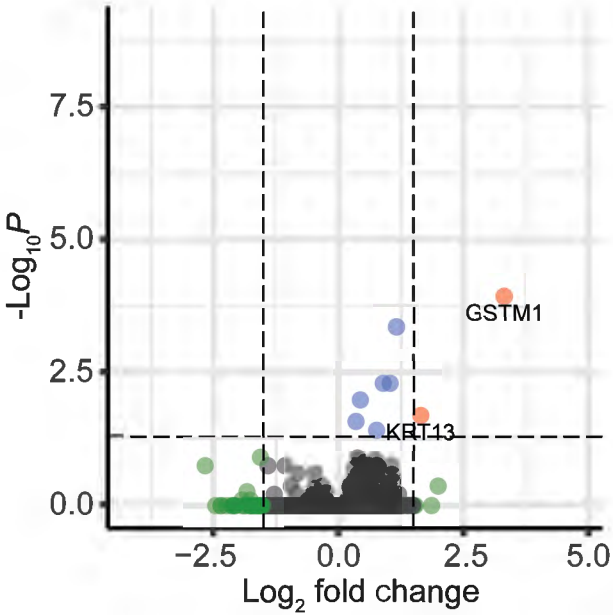
7.5
5.0
2.5
0.0
-Log10P
GSTM1
KRT13
−2.5
0.0
2.5
5.0
Log2 fold change

c

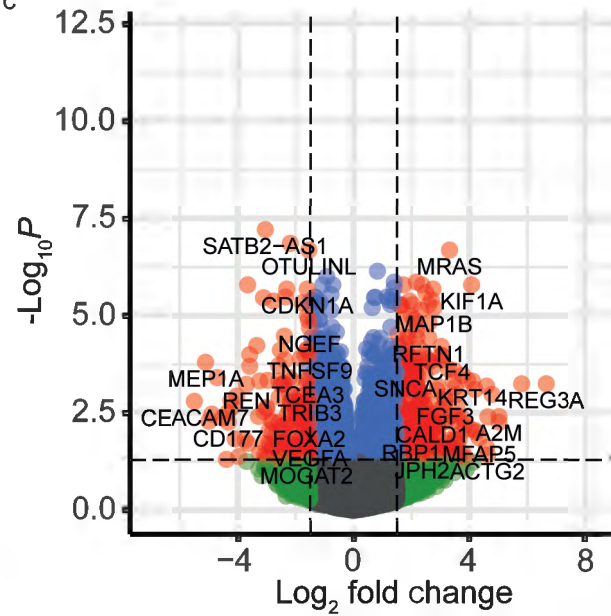
12.5
10.0
7.5
5.0
2.5
0.0
-Log10P
SATB2−AS1
OTULINL
CDKN1A
NGEF
TNFSF9
MEP1A
REN
TCEA3
CEACAM7
TRIB3
CD177
FOXA2
VEGFA
MOGAT2
MRAS
KIF1A
MAP1B
RFTN1
TCF4
SNCA
KRT14
REG3A
FGF3
CALD1
A2M
RBP1
MFAP5
JPH2
ACTG2
−4
0
4
8
Log2 fold change

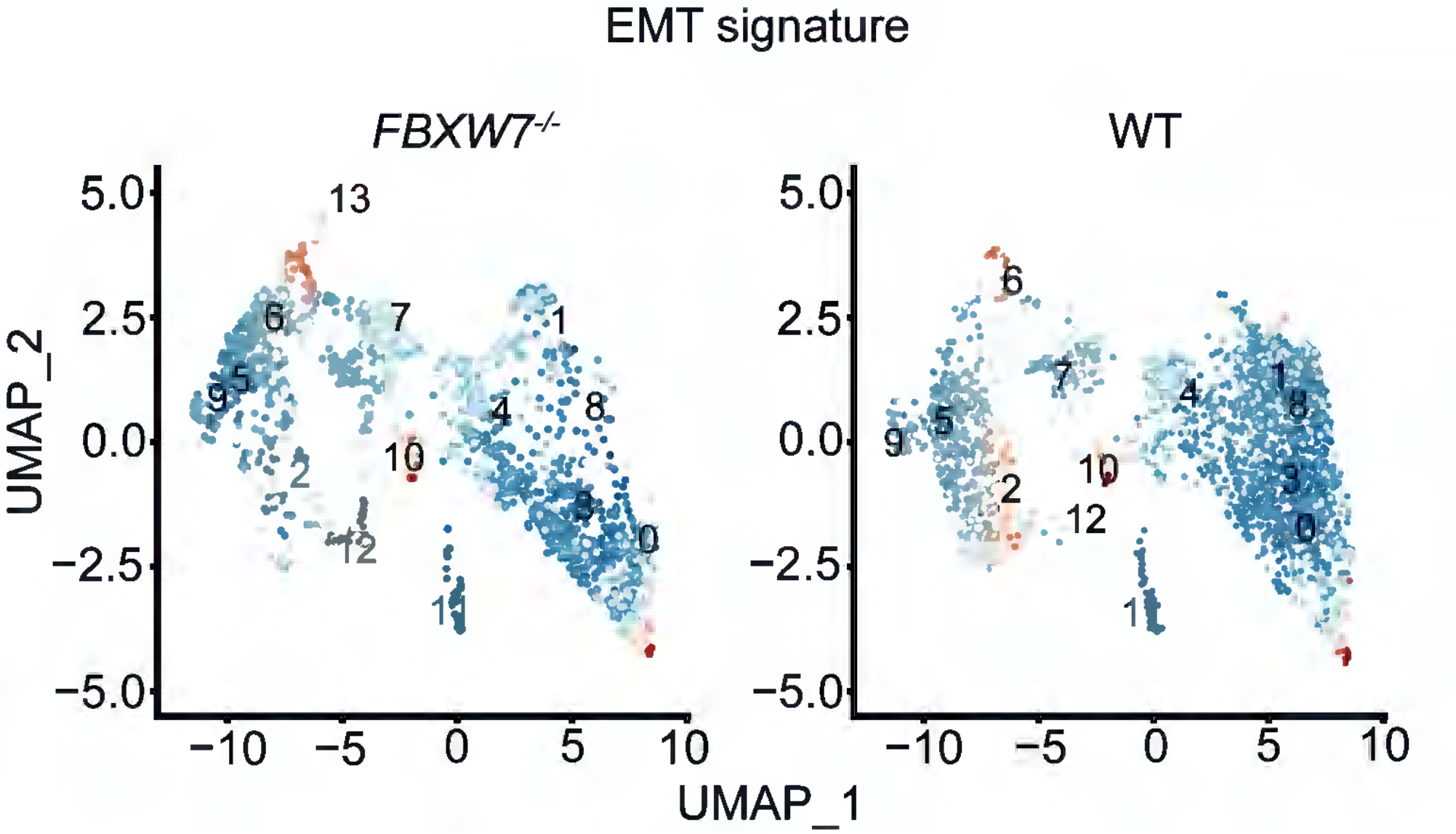
EMT signature
FBXW7-/-
WT
UMAP_2
UMAP_1
5.0
2.5
0.0
−2.5
−5.0
−10
−5
0
5
10
13
6
7
1
9
5
4
8
10
2
3
12
0
11

a

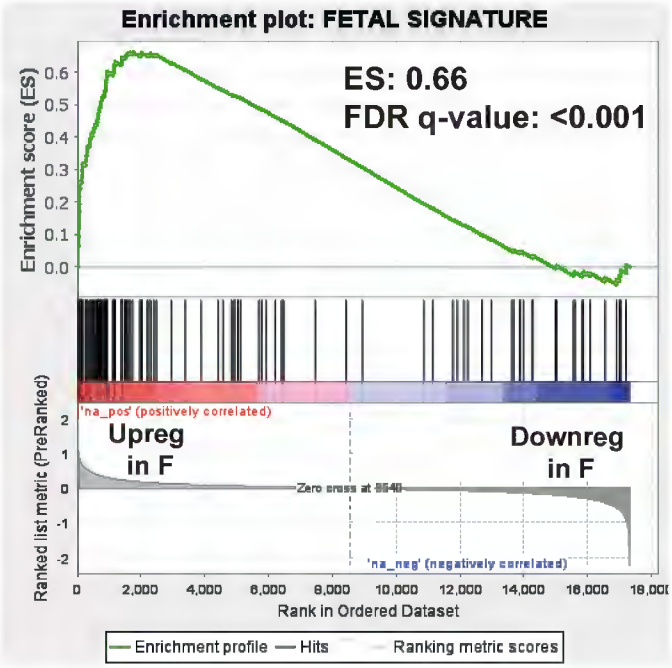
Enrichment plot: FETAL SIGNATURE
ES: 0.66
FDR q-value: <0.001
Enrichment score (ES)
'na_pos' (positively correlated)
Upreg in F
Downreg in F
Zero cross at 8548
'na_neg' (negatively correlated)
Ranked list metric (PreRanked)
Rank in Ordered Dataset
Enrichment profile
Hits
Ranking metric scores

b

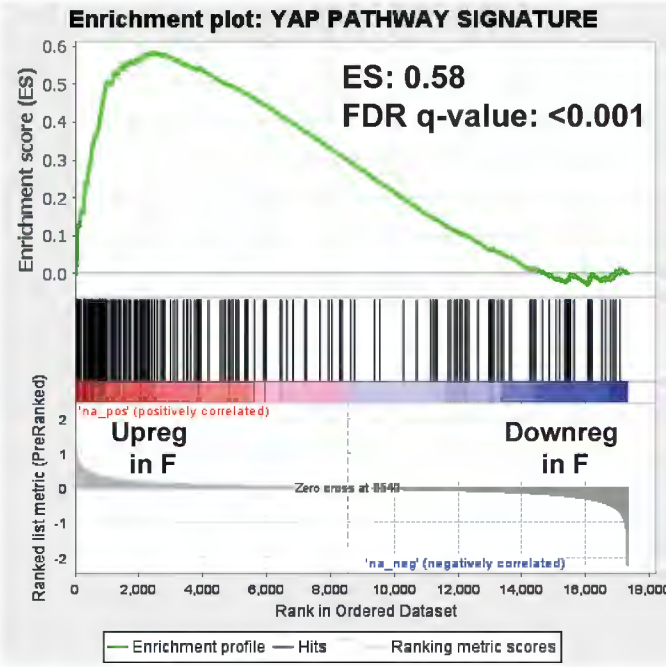
Enrichment plot: YAP PATHWAY SIGNATURE
ES: 0.58
FDR q-value: <0.001
Enrichment score (ES)
'na_pos' (positively correlated)
Upreg in F
Downreg in F
Zero cross at 8548
'na_neg' (negatively correlated)
Ranked list metric (PreRanked)
Rank in Ordered Dataset
Enrichment profile
Hits
Ranking metric scores

c

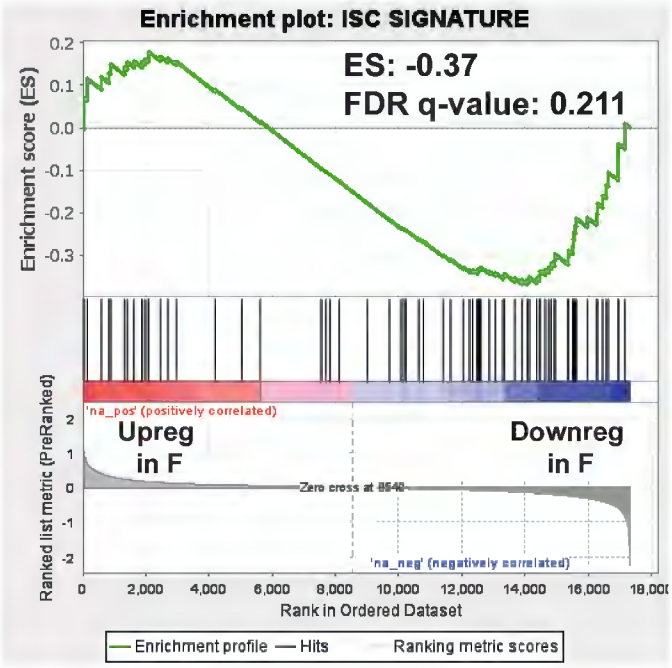
Enrichment plot: ISC SIGNATURE
ES: -0.37
FDR q-value: 0.211
Enrichment score (ES)
'na_pos' (positively correlated)
Upreg in F
Downreg in F
Zero cross at 8548
'na_neg' (negatively correlated)
Ranked list metric (PreRanked)
Rank in Ordered Dataset
Enrichment profile
Hits
Ranking metric scores

d

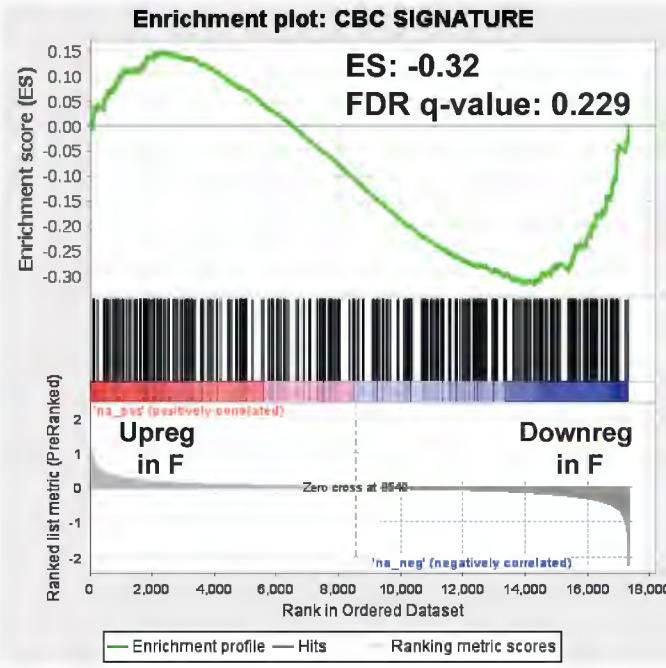
Enrichment plot: CBC SIGNATURE
ES: -0.32
FDR q-value: 0.229
Enrichment score (ES)
'na_pos' (positively correlated)
Upreg in F
Downreg in F
Zero cross at 8548
'na_neg' (negatively correlated)
Ranked list metric (PreRanked)
Rank in Ordered Dataset
Enrichment profile
Hits
Ranking metric scores

e

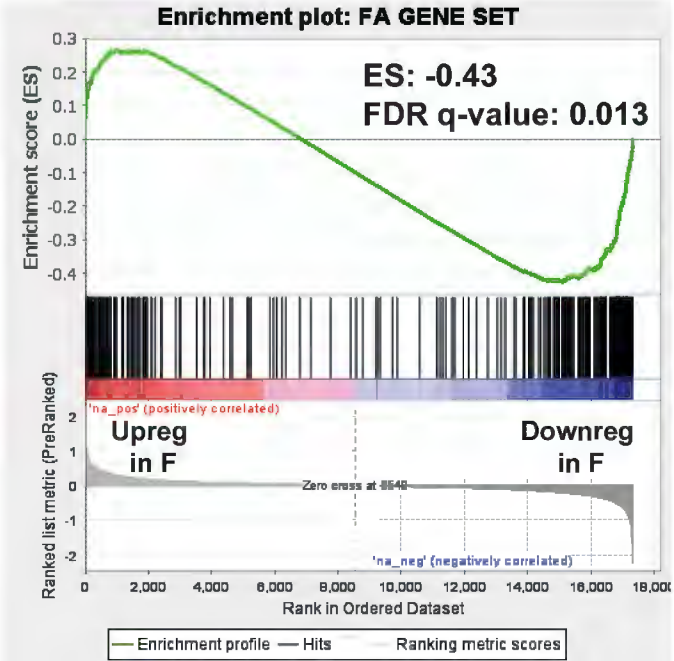
Enrichment plot: FA GENE SET
ES: -0.43
FDR q-value: 0.013
Enrichment score (ES)
'na_pos' (positively correlated)
Upreg in F
Downreg in F
Zero cross at 8548
'na_neg' (negatively correlated)
Ranked list metric (PreRanked)
Rank in Ordered Dataset
Enrichment profile
Hits
Ranking metric scores

a

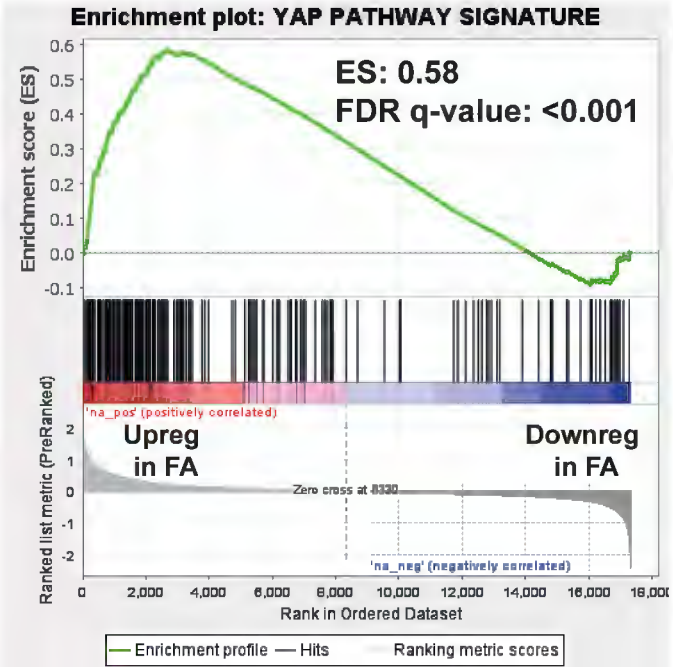
Enrichment plot: YAP PATHWAY SIGNATURE
ES: 0.58
FDR q-value: <0.001
Enrichment score (ES)
0.6
0.5
0.4
0.3
0.2
0.1
0.0
-0.1
'na_pos' (positively correlated)
Upreg
in FA
Downreg
in FA
Zero cross at 8330
'na_neg' (negatively correlated)
Ranked list metric (PreRanked)
2
1
0
-1
-2
0
2,000
4,000
6,000
8,000
10,000
12,000
14,000
16,000
18,000
Rank in Ordered Dataset
Enrichment profile
Hits
Ranking metric scores

b

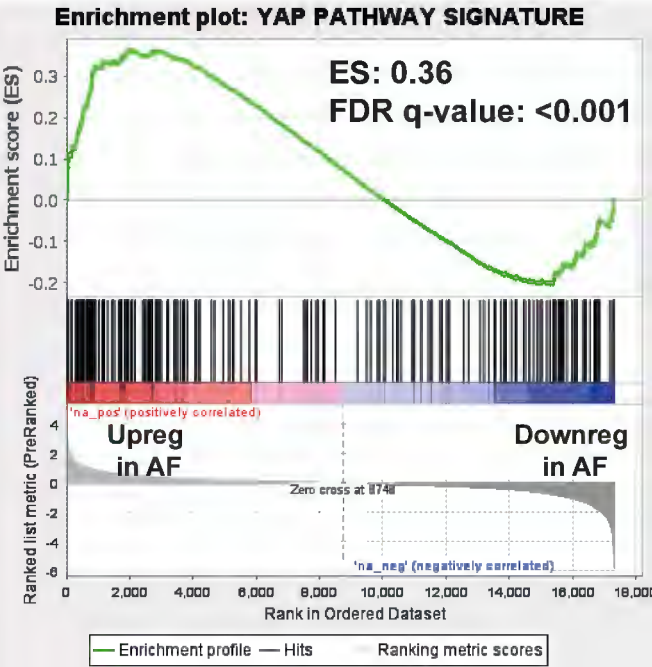
Enrichment plot: YAP PATHWAY SIGNATURE
ES: 0.36
FDR q-value: <0.001
Enrichment score (ES)
0.3
0.2
0.1
0.0
-0.1
-0.2
'na_pos' (positively correlated)
Upreg
in AF
Downreg
in AF
Zero cross at 8748
'na_neg' (negatively correlated)
Ranked list metric (PreRanked)
4
2
0
-2
-4
-6
0
2,000
4,000
6,000
8,000
10,000
12,000
14,000
16,000
18,000
Rank in Ordered Dataset
Enrichment profile
Hits
Ranking metric scores